Applied Acoustics 204 (2023) 109236

Contents lists available at ScienceDirect

Applied Acoustics

journal homepage: www.elsevier.com/locate/apacoust

Boundary conditions to represent the wave impedance characteristics of axial compressors

Bernhard Semlitsch *

Department of Fluid-Flow Machinery, TU Wien, Getreidemarkt 9, Vienna 1060 Austria
Whittle Laboratory, Department of Engineering, University of Cambridge, 1 JJ Thomson Avenue, Cambridge CB3 0DY, United Kingdom

ARTICLE INFO

Article history:
Received 9 July 2022
Received in revised form 4 January 2023
Accepted 20 January 2023

Keywords:
Acoustic networks
Boundary conditions
Compressor modelling
Thermo-acoustic instability

ABSTRACT

Thermo-acoustic oscillations can damage gas turbines. Numerical predictions guide the combustor design to prevent the occurrence of this hazardous resonance phenomenon. Uncertainties, such as incomplete knowledge of boundary conditions, challenge this strategy. For the appropriate estimation of combustor inlet boundary conditions, we develop a model mimicking the reflection characteristics of an axial compressor. The non-compact formulation relies on individual blade rows' performance data and allows thereby estimating the phase delay information. The evolution of the reflection coefficients is analysed for different operating conditions and related to the slope of the compressor characteristics. We find that the impedance at the compressor discharge varies significantly with frequency, resulting in wave interactions with all blade rows. Only towards compressor choke, high flow velocities at the compressor discharge restrict the penetration depth of incident waves resulting in reflection coefficients with minor frequency dependence. That even small phase components of the reflection coefficient are crucial for thermo-acoustic stability prediction is demonstrated in an example.

© 2023 The Author(s). Published by Elsevier Ltd. This is an open access article under the CC BY license (http://creativecommons.org/licenses/by/4.0/).

1. Introduction

The resonance of acoustic waves with unsteady heat release emitted by flames can severely damage gas turbines and, therefore, restricts the application of lean-burn combustion [1]. By predicting such thermo-acoustic instabilities, numerical simulations assist combustor design to reduce the oscillations to tolerable amplitudes. Prediction realism and uncertainty limit the design quality. Lamarque et al. [2], Bothien et al. [3], and Motheau et al. [4] demonstrated that boundary conditions can alter the thermo-acoustic characteristics of combustors. Hence, accurate models mimicking the acoustic characteristics of the combustor boundaries realistically are required for thermo-acoustic analysis.

Compressors embody the component upstream of the combustor in gas turbines condensing the working fluid. Their performance quantities are commonly displayed on maps as ratios to inflow and operating conditions, which are shown in Fig. 1 (a) for an axial compressor with six stages. The pressurisation response on a mass-flow rate alteration at the discharge can be read off in the quasi-steady limit. Hence, its acoustic reflection properties can be estimated accordingly to the slope of the compressor characteristic. The compressor characteristics at constant rotational speed become steep, especially at high rotational speeds. Thus, pressure oscillations, e.g. incident acoustic waves, entering at the compressor discharge cause only an insignificant mass-flow rate change at such operating conditions. Choked flow with a weak normal shock exhibits similar properties (corresponding to an infinite steepness), which is commonly assumed as an appropriate inflow boundary condition for the perturbation quantities. Choked inlet flow through a compact nozzle provides a defined acoustic boundary condition at minimal assumptions and is, therefore, also popular in laboratory experiments. Marble et al. [5] derived the reflection coefficient analytically for a compact choked nozzle while noting the importance of the phase shift of the reflected with respect to the incident wave in the second part of their work. Stow et al. [6] determined by an asymptotic analysis a higher-order correction of the reflection coefficient phase in the low-frequency limit. Duran et al. [7] found the reflection coefficients for any nozzle geometry using flow invariants. Despite the effort to establish boundary conditions for nozzle throats, handling the inlet boundary as choked nozzle flow might not be a suitable representation of an actual compressor. The flow is not necessarily choked there, and the waves might penetrate deep into the turbomachinery.

Boundary conditions mimicking the compressor need to be computationally efficient because numerous calculations are required at the combustor design stage. Acoustic boundary condi-

* Address: Department of Fluid-Flow Machinery, TU Wien, Getreidemarkt 9, Vienna 1060 Austria.
E-mail address: bernhard.semlitsch@tuwien.ac.at

https://doi.org/10.1016/j.apacoust.2023.109236
0003-682X/© 2023 The Author(s). Published by Elsevier Ltd.
This is an open access article under the CC BY license (http://creativecommons.org/licenses/by/4.0/).

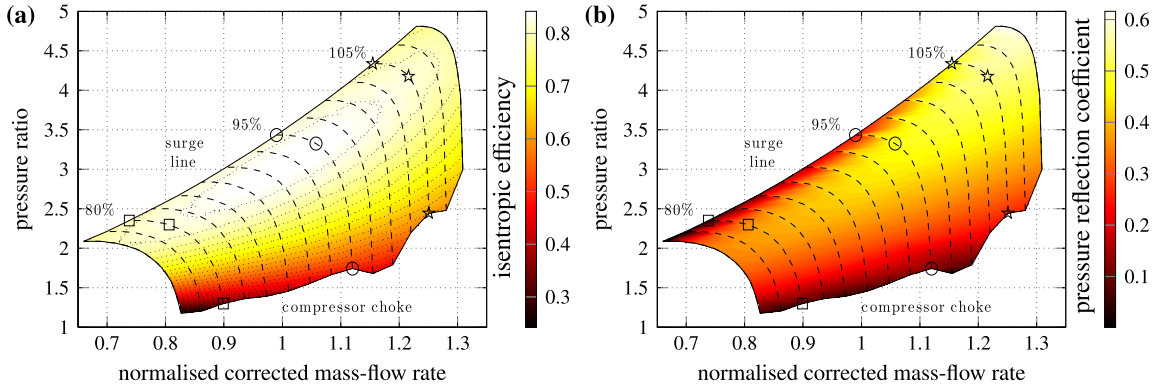

Fig. 1. Left: The performance of an axial high-pressure compressor is illustrated, where the contours indicate the isentropic efficiency. Right: Pressure reflection coefficient for incident waves at the compressor discharge as function of the operating condition.

tions for real combustors are challenging to measure experimentally because realistic operating conditions are hard to replicate. Lohse et al. [8] demonstrated that three-dimensional aeroacoustic simulations could calculate the acoustic reflection and transmission properties of a single compressor stage. However, the acoustic characterisation of several stages and frequencies by this methodology remains challenging due to limited computational resources. Moreover, the compressor might not be entirely designed yet, when the acoustic boundary conditions are required for combustor stability calculations. Silva et al. [9] developed a compact compressor boundary condition for thermo-acoustic limit cycle predictions solely based on the steepness of the pressure ratio performance map data at a constant rotational speed. An extended estimation procedure of the reflection coefficient, including the compressor temperature characteristics and the influence of the speed line derivatives, is described in Appendix A[1]. The pressure reflection coefficient for wave excitation at the compressor discharge thus obtained is shown in Fig. 1 (b). As a gas turbine component, compressors are operated along so-called running lines, which lay close to their optimal efficiency (provided adequate matching has been obtained). The variation range of reflection coefficients within such operating conditions is of interest because it determines the diversity of resonant modes.

The drawbacks of modelling the reflection properties with performance map data are that these relations are only valid in the quasi-steady limit (at zero frequency) and that the compressor is assumed to respond as a whole. Acoustic resonance phenomena [11] occurring between blade rows cannot be predicted with such methods. Axial, multistage compressors are not short compared to the incident acoustic wave. Therefore, propagation effects along blades need to be considered allowing phase shift evaluation.

With this work, a non-compact boundary condition formulation for axial compressors is presented, which is based on overall blade row performance data. The individual treatment of blade rows enables accurate phase shift determination at different frequencies. We investigate the reflection behaviour of an axial compressor, see Fig. 1, under different operating conditions and highlight the importance of the speed line derivative for the reflection coefficient. The impact of this boundary condition is demonstrated in a thermo-acoustic stability prediction with an acoustic network model. Within this example, we further illustrate the shortcomings of the choked flow inlet condition and the importance of the boundary condition phase on the modal growth rate.

[1] The effect of temperature gradients on the acoustic impedance has been revealed by Yeddula et al. [10].

2. Axial compressor boundary condition

Fast calculation procedures for boundary conditions are desired to enable efficient numerical simulations. Therefore, a low-order representation of an axial compressor, as suggested by Hynes [12], is employed. The simplifying assumptions are as follows; the hub to tip ratio is high such that radial fluctuations are negligible, the treatment of the blade flow as inclined channel flow with the stagger angle, γ_s, is adequate for the slightly curved passages, viscosity, and thermal conductivity do not influence the perturbation dynamics in a control volume, disturbances are sufficiently small to be represented by the linearised equations of fluid motion, which allows separate computation of mean and perturbation quantities.

The domain, representing the axial compressor geometry, is subdivided into propagation-alike segments. All control volumes start or terminate at a tip or trailing edge of a blade, which is illustrated in Fig. 2. (This treatment of blade rows as single control volumes implies that the mean flow quantities are thought to be constant in each of these control volumes.) The alternating arrangements of rotors and stators are represented by individual blade row control volumes, which inhibit circumferential flow between blade passages. In these, only propagation in the curved-linear coordinate system ξ (see Fig. 2 (b)) is considered. The interspace between blade rows is represented by bridging gap control volumes. In these, azimuthal flow is permitted and hence, an additional degree of freedom is considered. Actuator disks at the leading and trailing edges of blade rows form the interface between control volumes. These are computed based on conservation equations and empirical blade performance models, estimating the flow angle deviation and the pressure loss over a blade row. Thus, the calculation of the solution through the compressor is decomposed into propagation within control volumes and the modelling of interface conditions. Individual perturbation transmission matrices are formed from the gap volumes to the trailing edge of the consecutive blade row and combined to represent the entire compressor. The wave amplitudes are marched from the inlet through the whole domain and scaled appropriately to the imposed boundary conditions. At the compressor exit, the reflection coefficients are calculated and used as boundary condition in the thermo-acoustic simulations (See Fig. 3).

In Appendix B, a verification of the present implementation with data by Kaji et al. [13] is documented. Hynes [12] showed that the present low-order model is capable to predict compressor performance and stability. A comparison of the predicted transfer function with this model and experimental data has been presented by Knobloch et al. [14]. Worthwhile to note is that this

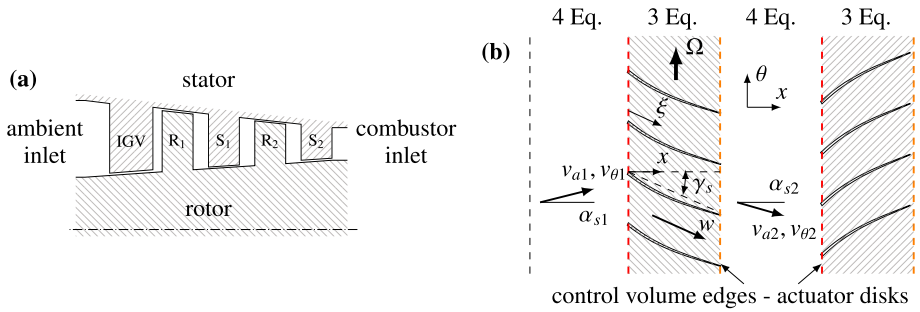

Fig. 2. Schematics of the numerical approach. Figure (a) illustrates the arrangement of control volumes of the rotor/stator assembly in an axial compressor and (b) shows a stage in detail.

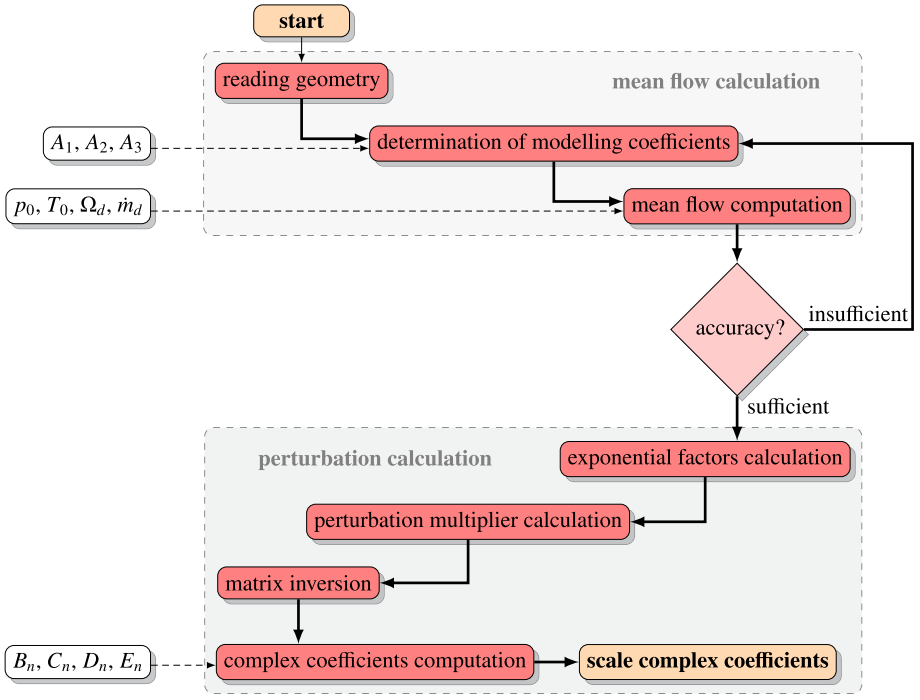

Fig. 3. Flow chart of the compressor model calculation procedure.

impedance boundary condition formulation can be also used in the time-domain when combined with the works by Rienstra [15] or Fung et al. [16]. Thus, the developed impedance boundary condition can also be used for Helmholtz solver or large eddy simulations.

2.1. Gap control volumes representing the space between rotor and stator rows

The governing equations are formulated in the cylindrical coordinate system (x, r, θ) due to the annular shape of the gaps and the possibility of azimuthal propagation. The four linearised conservation equations governing the behaviour of the primary perturbation quantities (indicated by primes), i.e. axial velocity v'_a, azimuthal velocity v'_θ, pressure p', and density ρ', in the gap control volumes can be written as,

$$\rho\frac{\partial v'_a}{\partial t}+\rho v_a\frac{\partial v'_a}{\partial x}+\rho\frac{v_\theta}{r}\frac{\partial v'_a}{\partial \theta}=-\frac{\partial p'}{\partial x} \tag{1}$$

for the axial momentum perturbation,

$$\rho\frac{\partial v'_\theta}{\partial t}+\rho v_a\frac{\partial v'_\theta}{\partial x}+\rho\frac{v_\theta}{r}\frac{\partial v'_\theta}{\partial \theta}=-\frac{1}{r}\frac{\partial p'}{\partial \theta} \tag{2}$$

for the circumferential momentum perturbation,

$$\frac{\partial \rho'}{\partial t}+\rho\frac{\partial v'_a}{\partial x}+\frac{\rho}{r}\frac{\partial v'_\theta}{\partial \theta}+v_a\frac{\partial \rho'}{\partial x}+\frac{v_\theta}{r}\frac{\partial \rho'}{\partial \theta}=0 \tag{3}$$

for the mass conservation, and

$$\frac{\partial s'}{\partial t}+v_a\frac{\partial s'}{\partial x}+\frac{v_\theta}{r}\frac{\partial s'}{\partial \theta}=0$$

for the entropy perturbation s'. Using the expression

$$s'=c_v(p'/p-\gamma\ \rho'/\rho),$$

with c_v being the specific heat capacity at constant volume, valid for a perfect gas, the equation can be transformed to

$$\frac{\partial p'}{\partial t}+v_a\frac{\partial p'}{\partial x}+\frac{v_\theta}{r}\frac{\partial p'}{\partial \theta}=a^2\left(\frac{\partial \rho'}{\partial t}+v_a\frac{\partial \rho'}{\partial x}+\frac{v_\theta}{r}\frac{\partial \rho'}{\partial \theta}\right), \tag{4}$$

where a is the speed of sound. The density fluctuations ρ' are related to pressure fluctuations by $p'=a^2\rho'$. This system of four differential equations describes the evolution of the primary disturbance variables. Since the mean flow quantities and the geometrical constrains are known, solutions for the disturbance variables can be found by Fourier superposition. Therefore, we first

differentiate Eq. (1) with respect to x and Eq. (2) with respect to θ, which gives

$$\left(\rho\frac{\partial}{\partial t}+\rho v_a\frac{\partial}{\partial x}+\rho\frac{v_\theta}{r}\frac{\partial}{\partial\theta}\right)\frac{\partial v'_a}{\partial x}=-\frac{\partial^2 p'}{\partial x^2}, \tag{5}$$

and

$$\left(\rho\frac{\partial}{\partial t}+\rho v_a\frac{\partial}{\partial x}+\rho\frac{v_\theta}{r}\frac{\partial}{\partial\theta}\right)\frac{\partial v'_\theta}{\partial\theta}=-\frac{1}{r}\frac{\partial^2 p'}{\partial\theta^2}. \tag{6}$$

Dividing Eq. (6) by r and adding Eq. (5) gives,

$$\left(\rho\frac{\partial}{\partial t}+\rho v_a\frac{\partial}{\partial x}+\rho\frac{v_\theta}{r}\frac{\partial}{\partial\theta}\right)\left(\frac{\partial v'_a}{\partial x}+\frac{1}{r}\frac{\partial v'_\theta}{\partial\theta}\right)=-\left(\frac{\partial^2 p'}{\partial x^2}+\frac{1}{r^2}\frac{\partial^2 p'}{\partial\theta^2}\right). \tag{7}$$

The term, $\frac{\partial v'_a}{\partial x}+\frac{1}{r}\frac{\partial v'_\theta}{\partial\theta}$, can be replaced using the mass conservation Eq. (3) leading to

$$\frac{\partial^2 p'}{\partial x^2}+\frac{1}{r^2}\frac{\partial^2 p'}{\partial\theta^2}=\frac{1}{a^2}\left(\frac{\partial}{\partial t}+v_a\frac{\partial}{\partial x}+\frac{v_\theta}{r}\frac{\partial\rho'}{\partial\theta}\right)^2 p', \tag{8}$$

where v_a/a is the axial Mach number, M_a, and v_θ/a is the azimuthal Mach number, M_θ. The solution to this equation can be found by separation of variables. A Fourier superposition of solutions of the form $p'=f(x)\ \exp(i\omega t+in\theta)$ is substituted in the Eq. (8),

$$\left(1-M_a^2\right)\frac{d^2 f(x)}{dx^2}-2iM_a\left(\frac{\omega}{a}+\frac{n}{r}M_\theta\right)\frac{df(x)}{dx}+\left(\left(\frac{\omega}{a}+\frac{n}{r}M_\theta\right)^2-\frac{n^2}{r^2}\right)f(x)=0. \tag{9}$$

The angular frequency is ω and n is the circumferential harmonic of distortion. The solutions to this equation are proportional to $\exp(i\beta x/r)$. The complex axial wavenumbers are,

$$\beta_{1,2}=\frac{M_a\left(\frac{\omega r}{a}+nM_\theta\right)}{1-M_a^2}\pm\frac{i\sqrt{\left(n^2\left(1-M_a^2\right)-\left(\frac{\omega r}{a}+nM_\theta\right)^2\right)}}{1-M_a^2}. \tag{10}$$

With complex coefficients, i.e. B_n, C_n, the evolution of the pressure fluctuations can be obtained,

$$\frac{p'}{p}=\gamma\sum_{n=0}^{\infty}\left(\left(\frac{\omega r}{a}+\beta_1 M_a+nM_\theta\right)B_n e^{i\varphi}+\left(\frac{\omega r}{a}+\beta_2 M_a+nM_\theta\right)C_n e^{i\psi}\right). \tag{11}$$

The exponential factors are,

$$\varphi=\omega t+n\theta+\beta_1\frac{x}{r}\qquad\text{and}\qquad\psi=\omega t+n\theta+\beta_2\frac{x}{r}. \tag{12}$$

These complex coefficients are to be determined with the inlet and outlet boundary conditions of the compressor.

An additional solution for density fluctuations ρ' arises, which corresponds to entropy waves. These solutions satisfy the condition,

$$\left(\frac{\partial}{\partial t}+v_a\frac{\partial}{\partial x}+\frac{v_\theta}{r}\frac{\partial}{\partial\theta}\right)\rho'=0. \tag{13}$$

The multiplication with r/a reveals that the solutions to Eq. (13) are proportional to

$$e^{-i\left(\frac{\omega r}{a}+nM_\theta\right)/M_a\cdot x/r}.$$

Hence, the density fluctuations are given by,

$$\frac{\rho'}{\rho}=\frac{1}{\gamma}\frac{p'}{p}+\sum_{n=0}^{\infty}E_n e^{i\chi}, \tag{14}$$

with an additional complex coefficient, E_n, where

$$\chi=\omega t+n\theta-\frac{\frac{\omega r}{a}+nM_\theta}{M_a}\frac{x}{r}. \tag{15}$$

In order to obtain solutions for v_a and v_θ, the solutions for p' and ρ' are substituted into the Eqs. (1)–(3). Additional solutions can be found for $p'=0$ and $\rho'=0$ corresponding to pure vorticity waves. The axial velocity normalised by the speed of sound a is,

$$\frac{v'_a}{a}=\sum_{n=0}^{\infty}\left(-\beta_1 B_n e^{i\varphi}-\beta_2 C_n e^{i\psi}+nM_a D_n e^{i\chi}\right) \tag{16}$$

and the azimuthal velocity normalised by the speed of sound is,

$$\frac{v'_\theta}{a}=\sum_{n=0}^{\infty}\left(-nB_n e^{i\varphi}-nC_n e^{i\psi}+\left(\frac{\omega r}{a}+nM_\theta\right)D_n e^{i\chi}\right) \tag{17}$$

where D_n is another complex coefficient.

The solutions for the total pressure,

$$p_0=p\left(1+\frac{\gamma-1}{2}M^2\right)^{\frac{\gamma}{\gamma-1}},$$

and total temperature,

$$T_0=T\left(1+\frac{\gamma-1}{2}M^2\right),$$

can be written as,

$$\frac{p'_0}{p_0}=\frac{\gamma}{1+\frac{\gamma-1}{2}M^2}\sum_{n=0}^{\infty}\left(\frac{\omega r}{a}B_n e^{i\varphi}+\frac{\omega r}{a}C_n e^{i\psi}+\left[nM_a^2+M_\theta\left(\frac{\omega r}{a}+nM_\theta\right)\right]D_n e^{i\chi}+\frac{M^2}{2}E_n e^{i\chi}\right) \tag{18}$$

and

$$\frac{T'_0}{T_0}=\frac{\gamma-1}{1+\frac{\gamma-1}{2}M^2}\sum_{n=0}^{\infty}\left(\frac{\omega r}{a}B_n e^{i\varphi}+\frac{\omega r}{a}C_n e^{i\psi}+\left[nM_a^2+M_\theta\left(\frac{\omega r}{a}+nM_\theta\right)\right]D_n e^{i\chi}-\frac{1}{\gamma-1}E_n e^{i\chi}\right). \tag{19}$$

The solution for the flow angle, α_s, is derived from the Kutta condition and can be written as,

$$\frac{\tan(\alpha_s)'}{\tan(\alpha_s)}=\sum_{n=0}^{\infty}\left(\left(\frac{\beta_1}{M_a}-\frac{n}{M_\theta}\right)B_n e^{i\phi}+\left(\frac{\beta_2}{M_a}-\frac{n}{M_\theta}\right)C_n e^{i\psi}+\frac{\omega r}{a}D_n e^{i\chi}\right). \tag{20}$$

2.2. Blade-row control volumes

The blades outline curved channels and thereby inhibit circumferential flow. Hence, only three linearised conservation equations govern the perturbation behaviour in the blade row volumes, which can be written in curved-linear coordinate system ξ as,

$$\rho\frac{\partial w'}{\partial t}+\rho w\frac{\partial w'}{\partial\xi}=-\frac{\partial p'}{\partial\xi}, \tag{21}$$

for the flow momentum,

$$\frac{\partial\rho'}{\partial t}+w\frac{\partial\rho'}{\partial\xi}=-\rho\frac{\partial w'}{\partial\xi} \tag{22}$$

for the mass conservation equation, and as

$$\frac{\partial p'}{\partial t}+w\frac{\partial p'}{\partial\xi}=a^2\left(\frac{\partial\rho'}{\partial t}+w\frac{\partial\rho'}{\partial\xi}\right), \tag{23}$$

for the energy or entropy conservation equation. The solutions to this equation system can be written as,

$$\frac{p'}{p}=\gamma\sum_{n=0}^{\infty}\left(\widetilde{B_n}e^{i\widetilde{\varphi}}+\widetilde{C_n}e^{i\widetilde{\psi}}\right), \tag{24}$$

for the pressure fluctuation,

$$\frac{\rho'}{\rho} = \frac{1}{\gamma}\frac{p'}{p} + \sum_{n=0}^{\infty} \widetilde{E}_n e^{i\widetilde{\chi}}, \tag{25}$$

for the density fluctuation, and

$$\frac{w'}{a} = \sum_{n=0}^{\infty} \left(-\widetilde{B}_n e^{i\widetilde{\varphi}} + \widetilde{C}_n e^{i\widetilde{\psi}} \right) \tag{26}$$

for the velocity perturbation. The solutions for the total pressure and total temperature can be written as,

$$\frac{p'_0}{p_0} = \sum_{n=0}^{\infty} \left(\frac{\gamma(1-M_\xi)}{1+\frac{\gamma-1}{2}M_\xi^2} \widetilde{B}_n e^{i\phi} + \frac{\gamma(1+M_\xi)}{1+\frac{\gamma-1}{2}M_\xi^2} \widetilde{C}_n e^{i\psi} + \frac{M_\xi^2}{2} \frac{\gamma}{1+\frac{\gamma-1}{2}M_\xi^2} \widetilde{E}_n e^{i\chi} \right) \tag{27}$$

and

$$\frac{T'_0}{T_0} = \sum_{n=0}^{\infty} \left(\frac{(\gamma-1)(1-M_\xi)}{1+\frac{\gamma-1}{2}M_\xi^2} B_n e^{i\phi} + \frac{(\gamma-1)(1+M_\xi)}{1+\frac{\gamma-1}{2}M_\xi^2} C_n e^{i\psi} - \frac{1}{1+\frac{\gamma-1}{2}M_\xi^2} E_n e^{i\chi} \right). \tag{28}$$

The exponential factors are

$$\widetilde{\varphi} = (\omega + n\Omega)t + \frac{(\omega+n\Omega)r}{(1-M_\xi)a}\frac{\xi}{r}, \tag{29}$$

$$\widetilde{\psi} = (\omega + n\Omega)t - \frac{(\omega+n\Omega)r}{(1+M_\xi)a}\frac{\xi}{r}, \tag{30}$$

$$\widetilde{\chi} = (\omega + n\Omega)t - \frac{(\omega+n\Omega)r}{(M_\xi)a}\frac{\xi}{r}, \tag{31}$$

where Ω is the rotational speed of the engine. For the stator rows, Ω is zero and vanishes from the equations above.

The solutions are presented in the rotating reference frame. Hence, a coordinate transformation needs be performed to interface the equation systems for the blade row and gap control volumes,

$$\xi\ \cos(\gamma_s) = x \qquad \text{and} \qquad \xi\ \sin(\gamma_s) = r(\theta - \Omega t). \tag{32}$$

Eliminating Ωt and ξ from Eqs. (29)–(31), the exponential factors become,

$$\widetilde{\varphi} = \omega t + n\theta - n\ \tan(\gamma_s)\frac{x}{r} + \frac{(\omega+n\Omega)r}{(1-M_\xi)a}\frac{x}{r\ cos(\gamma_s)}, \tag{33}$$

$$\widetilde{\psi} = \omega t + n\theta - n\ \tan(\gamma_s)\frac{x}{r} - \frac{(\omega+n\Omega)r}{(1+M_\xi)a}\frac{x}{r\ cos(\gamma_s)}, \tag{34}$$

$$\widetilde{\chi} = \omega t + n\theta - n\ \tan(\gamma_s)\frac{x}{r} - \frac{(\omega+n\Omega)r}{(M_x)a}\frac{x}{r}. \tag{35}$$

Again, the complex coefficients, i.e. $\widetilde{B}_n$, $\widetilde{C}_n$, and $\widetilde{E}_n$, need to be determined such that the boundary conditions are satisfied.

2.3. Actuator disks interfacing gap and blade-row control volumes

Interface conditions for wave amplitudes need to be fulfilled while being transported from one control volume into the next. At the leading edge of blade rows (which has been marked in red colour in Fig. 2 (b)), the mass flux, total pressure and total temperature perturbations need to be conserved between the upstream, 1, and downstream, 2, volume,

$$\frac{\rho'_1}{\rho_1} + \frac{v'_1}{v_1} = \frac{\rho'_2}{\rho_2} + \frac{w'_2}{w_2} \tag{36}$$

$$T'_{0,1} = T'_{0,2} \tag{37}$$

$$p'_{0,1} = p'_{0,2}. \tag{38}$$

At the trailing edge of blade rows (marked in orange colour in Fig. 2 (b)), an additional condition is required for the four conservation equations in the gap control volume. The mass flux and total enthalpy perturbations are conserved also at this trailing edge interface,

$$\frac{\rho'_1}{\rho_1} + \frac{w'_1}{w_1} = \frac{\rho'_2}{\rho_2} + \frac{v'_2}{v_2} \tag{39}$$

$$T'_{0,1} = T'_{0,2}. \tag{40}$$

Total pressure losses manifest over blade rows and hence, the total pressure perturbation amplitudes are not conserved. An empirical formulation suggested by Emmons et al. [17] is used to model the blade row performance with the blade row loss coefficient $\overline{\varepsilon_L}$ as a function of inflow quantities, i.e. the Mach number at the leading edge, M_1, and flow incidence angle, α_{s1},

$$\overline{\varepsilon_L}(\tan(\alpha_{s1}), M_1) = \frac{p_{0,1} - p_{0,2}}{p_{0,1} - p_1} = A_1 \left(1 + A_2 \left(\frac{\alpha_{s1} - \alpha_{opt,1}}{\epsilon_{opt}} \right)^2 \right), \tag{41}$$

where A_1 and A_2 are modelling coefficients, $\alpha_{opt,1}$ is the mid-radius incidence angle at minimum loss and ϵ_{opt} is the optimum deflection. The amplitude of the total pressure perturbation at the tailing edge can computed by the perturbations inserted in Eq. (41), i.e. $p'_{0,1} - \left(p'_{0,1} - p'_1\right)\overline{\varepsilon_L}$, plus the contribution of the inflow quantity perturbations, i.e. the Mach number at the leading edge, M'_1, and flow incidence angle, $\tan(\alpha_{s1})'$, changing the loss coefficient, $\overline{\varepsilon_L}$. Emmons et al. [17] showed that the time delay of the total pressure perturbation over a blade row is influenced by the boundary layer development on the blades. The effect of a generated eddy on the boundary layer is delayed by the time τ due to the convection with the mean flow in the blade passage and the time dependence is represented as the phase delay (i.e. $1 + i(\omega + n\Omega)\tau$) of the total pressure perturbation at the trailing edge. For an exponential time dependence, representing the unsteady nature of a small disturbance propagation, this leads to the formulation [18],

$$p'_{0,2} = p'_{0,1} - \frac{1}{1+i(\omega+n\Omega)\tau}\left(\left(p'_{0,1} - p'_1\right)\overline{\varepsilon_L} + (p_{0,1} - p_1)\left(\frac{\partial\overline{\varepsilon_L}}{\partial\tan(\alpha_{s1})}\tan(\alpha_{s1})' + \frac{\partial\overline{\varepsilon_L}}{\partial M_1}M'_1 \right) \right). \tag{42}$$

As similarly suggested by Lieblein [19], the influence of the flow incidence angle α_{s1} on the flow deflection angle α_{s2} is modelled by,

$$\alpha_{s2} = A_3 \cdot \left(\alpha_{s1} - \alpha_{opt,1}\right) + \alpha_{opt,2}, \tag{43}$$

where A_3 is the deviation factor, and $\alpha_{opt,2}$ is the flow angle at minimum loss measured at the mid-radius exit. The modelling coefficients, A_1, A_2, and A_3, can be obtained from textbooks for certain blade profiles or are calibrated with experimental mean flow data such that a compressor performance map can be reproduced. Therefore, these coefficients represent scaling parameters to match the compressor characteristics.

The flow deflection angle amplitude at the trailing edge can be derived by calculating its derivative with respect to the inflow quantities, i.e. the Mach number at the leading edge, M_1, and flow incidence angle, $\tan(\alpha_{s1})$, and multiplying with the corresponding inflow perturbations. The propagation nature of the flow deflection angle over the blade row can be modelled as phase delay by the time τ due to the convection with the mean flow in the blade passage, as shown by Emmons et al. [17]. Thus, the relation describing the convection of flow angle perturbations over a blade row can be derived from the steady-state leaving angle relation,

$$\tan(\alpha_{s2})' = \frac{1}{1+i(\omega+n\Omega)\tau}\cdot\left(\frac{\partial\tan(\alpha_{s2})}{\partial\tan(\alpha_{s1})}\tan(\alpha_{s1})' + \frac{\partial\tan(\alpha_{s2})}{\partial M_1}M_1'\right). \tag{44}$$

M_a and M_θ are the axial and the circumferential Mach-numbers based on the mean flow velocity components, respectively. This implies that

$$M_a' = v_a'/a + M_a/2(\rho'/\rho - p'/p).$$

2.4. Solving the equation system describing the compressor

The equation system defined by the three interface conditions at the leading edge of a blade row, i.e. Eqs. (36)–(38), can be written as,

$$\begin{pmatrix} b_{1,1} & b_{1,2} & b_{1,3} & b_{1,4} \\ b_{2,1} & b_{2,2} & b_{2,3} & b_{2,4} \\ b_{3,1} & b_{3,2} & b_{3,3} & b_{3,4} \end{pmatrix} \begin{pmatrix} B_n e^{\varphi} \\ C_n e^{\psi} \\ D_n e^{\chi} \\ E_n e^{\chi} \end{pmatrix}^{j} = \begin{pmatrix} c_{1,1} & c_{1,2} & c_{1,3} \\ c_{2,1} & c_{2,2} & c_{2,3} \\ c_{3,1} & c_{3,2} & c_{3,3} \end{pmatrix} \begin{pmatrix} \widetilde{B}_n \\ \widetilde{C}_n \\ \widetilde{E}_n \end{pmatrix}^{j+1}, \tag{45}$$

where the left and right hand side represents the perturbation amplitudes of the waves (four in the j^{th} control volume) just upstream and (three in the $j^{th}+1$ control volume) downstream of the leading edge, respectively. The matrices entries are determined by the constants preceding the individual complex coefficients in Eqs. (14), (16), (18) and (19) for the left hand side and Eqs. (25)–(28) for the right hand side. On the left hand side, the convection delay in the gap in between blade rows is accounted for by exponential factors. The corresponding equation system for the trailing edge can be formed by the four conditions, i.e. Eqs. (39), (40), (42), and (43)

$$\begin{pmatrix} c_{1,1} & c_{1,2} & c_{1,3} \\ c_{2,1} & c_{2,2} & c_{2,3} \\ c_{3,1} & c_{3,2} & c_{3,3} \\ 0 & 0 & 0 \end{pmatrix} \begin{pmatrix} \widetilde{B}_n e^{\widetilde{\varphi}} \\ \widetilde{C}_n e^{\widetilde{\psi}} \\ \widetilde{E}_n e^{\widetilde{\chi}} \end{pmatrix}^{j+1} + \begin{pmatrix} 0 & 0 & 0 & 0 \\ 0 & 0 & 0 & 0 \\ \Delta p_1 & \Delta p_2 & \Delta p_3 & \Delta p_4 \\ \Delta\alpha_{s,1} & \Delta\alpha_{s,2} & \Delta\alpha_{s,3} & \Delta\alpha_{s,4} \end{pmatrix} \begin{pmatrix} B_n e^{\varphi} \\ C_n e^{\psi} \\ D_n e^{\chi} \\ E_n e^{\chi} \end{pmatrix}^{j} = \begin{pmatrix} d_{1,1} & d_{1,2} & d_{1,3} & d_{1,4} \\ d_{2,1} & d_{2,2} & d_{2,3} & d_{2,4} \\ d_{3,1} & d_{3,2} & d_{3,3} & d_{3,4} \\ d_{4,1} & d_{4,2} & d_{4,3} & d_{4,4} \end{pmatrix} \begin{pmatrix} B_n \\ C_n \\ D_n \\ E_n \end{pmatrix}^{j+2}, \tag{46}$$

where the first term on the left and the right hand side represent the perturbation amplitudes right upstream and downstream of the trailing edge, respectively. The second term on the left hand side accounts for the total pressure losses Δp_i (see Eq. (42)) and transferred flow angle perturbations $\Delta\alpha_{s,i}$ (see Eq. (44)), which is formulated in terms of the perturbation amplitudes of the preceding gap control volume. Again, the matrix entries correspond to the constants preceding the individual complex coefficients in Eqs. (25)–(28) for the left hand side and Eqs. (14), (16), (18), (19), and (20) for the right hand side. Elimination of the blade row perturbation amplitudes by combining the equation systems 45 and 46, a four by four transmission matrix can be obtained relating the complex coefficients in the present with the consecutive gap control volume.

This equation system describing the transmission and reflection properties of the perturbation amplitudes always takes this corresponding matrix form in blade row and gap control volumes. These matrices can be built for each blade row and stored. Combining the transfer matrices for all blade rows, the transmission and the reflection behaviour of the compressor is defined. The boundary conditions are that no pressure, vorticity and entropy waves enter the domain through the inlet, while a pressure wave enters at the compressor exit. All other wave amplitudes are to be determined.

Table 1
Interpretation of the terms associated with complex coefficients.

Physical interpretation of the terms	Gap	Blade row
Upstream decaying potential modes	B_n	$\widetilde{B}_n$
Downstream growing potential modes	C_n	$\widetilde{C}_n$
Vorticity modes	D_n	-
Entropy modes	E_n	$\widetilde{E}_n$

An initial guess is propagated from the inlet through all blade rows of the compressor accounting for the boundary conditions of particular wave amplitudes. Generally, the result at the outlet boundary will not satisfy the outlet boundary conditions, but the wave amplitudes can be scaled correspondingly due to the linearity of the problem.

Terms associated with particular complex coefficients can be related to physical propagation phenomena and are listed in Table 1. Contributions with the complex coefficients B_n and C_n are potential modes representing upstream and downstream propagation, respectively. Due to the nature of the Eqs. (11) and (24), these modes are often considered as pressure modes. The upstream wave propagation terms are crucial, because only these can cause coupling of compressor segments. The terms involving complex coefficients D_n can be regarded as vorticity waves and terms with complex coefficients E_n can be seen as entropy waves. Vorticity waves are not transported through blade rows, since only three degrees of freedom are considered.

2.5. Application of the compressor model

Firstly, the geometry of the compressor has to be specified, which consists for each blade row of the axial coordinates of the blade's leading and tailing edges, the hub and casing radius at the exit, the blockage factor, the mid-radius stagger angle, the mid-radius inlet and outlet angle at minimum loss, the optimum deflection angle, and the minimum value of the loss coefficient. The modelling coefficients, A_1, A_2, and A_3, are fitted for each blade row to match empirical correlations for the profiles, which can be obtained experimentally or from literature.[2] The aforementioned procedure is best suited during the design stage of the compressor. The modelling coefficients can be matched to represent the compressor performance map if the compressor exists.

The total pressure and total temperature are set at the inlet as mean flow boundary conditions. The compressor operating map is calculated with a given rotational design speed, Ω_d, and design mass-flow rate, $\dot{m}_d$, for a range of rotational speeds. With the determined mean flow, the exponential factors, representing the mode decay with axial distance, and the perturbation multipliers can be evaluated. The matrices, i.e. representing the interface conditions, can be formed and inverted to explicitly solve the set of equations.

The complex coefficients are set at the inflow accordingly to the present perturbations. For the remainder of the investigation, it is assumed that no perturbations enter the compressor, but upstream propagating acoustic waves leave the compressor inlet. Hence, the initial conditions at the compressor inlet are $B_n = 1$ and $C_n = D_n = E_n = 0$. This inlet condition for the complex coefficients is propagated downstream by solving the system of equations. The initial result will generally not fulfil the boundary condition at the compressor outlet. Because of the problem linearity, the wave amplitudes can be scaled appropriately, e.g. the forcing amplitudes obtained by a thermo-acoustic simulation.

[2] Models for the loss and deviation factors are constantly improving (e.g. König et al. [20], Banjac et al. [21], or Ferrer et al. [22]), where the best representation should be applied to obtain the most accurate results.

3. Results

Firstly, an individual blade row is investigated to demonstrate the modelling implications on the wave transmission and reflection properties. The acoustic energy flux rates for an upstream travelling pressure wave can be analysed in terms of acoustic energy coefficients;

$$R^- = \frac{\hat{p}_2^+}{\hat{p}_2^-} = \frac{\left(1+\overline{M_2}\right)^2}{\left(1-\overline{M_2}\right)^2}\left|\frac{C_{0,2}}{B_{0,2}}\right|^2 \tag{47}$$

$$T^- = \frac{\hat{p}_1^-}{\hat{p}_2^-} = \frac{\mathcal{A}_1}{\mathcal{A}_2}\frac{\overline{\rho_2 a_2}}{\overline{\rho_1 a_1}}\frac{\left(1-\overline{M_1}\right)^2}{\left(1-\overline{M_2}\right)^2}\cdot\left|\frac{p_1\left(\frac{\omega r}{a}+\beta_1 M_a\right)_1}{p_2\left(\frac{\omega r}{a}+\beta_1 M_a\right)_2}\frac{B_{0,1}}{B_{0,2}}\right|^2, \tag{48}$$

where R^- is the reflected and T^- is the transmitted acoustic energy coefficient through the cascade, the hat on the pressure indicates that only the acoustic pressure is considered, $\mathcal{A}$ is the cross-sectional area, and the indices 1 and 2 indicate the upstream and downstream location, respectively.

Given that no vorticity and entropy waves are imposed at the compressor inlet, it is worthwhile to note that no vorticity or entropy waves are generated when A_1 and A_3 are set to zero because the total pressure losses Δp_i and transferred flow angle perturbations $\Delta\alpha_{s,i}$ in Eq. (46) vanish. With these modelling coefficients being zero, the blades act simply as guide vanes, and the acoustic energy flux is conserved (as shown in Fig. 4 (a), which shows the magnitudes of the acoustic energy reflection and transmission coefficient). The rotor rotation is ideal and alters the mean flow quantities without losses. The larger the rotational speed of the blade row, the larger are the changes in the mean flow quantities, which cause the reflection of the injected waves at the blade row.

A realistic blade row causes losses and induces, thereby, vorticity and entropy waves. With their formation, the acoustic energy flux is no longer conserved over a blade row, as shown in Figs. 4 (b) and (c) illustrating that $|T^-|+|R^-|$ is not strictly one. The coefficient A_1 determines the pressure loss over a blade row and the deviation factor, A_3, adjusts the Kutta condition. The Eqs. (42) and (44) define the scaling relations of these coefficients, A_1 and A_3, and the amplitudes of entropy and vorticity waves, respectively. These two equations distinguish each other essentially by a zero-order term and the sign. First-order derivative terms, representing the impact of a flow incidence angle or Mach number change, define intricately the proportion of wave amplitudes generated. Both essential quantities, the flow deflection angle, α_{s2}, and the blade row loss coefficient, $\overline{\varepsilon_L}$, scale with the difference (or the quadratic difference) of the actual α_{s1} and optimal flow incidence $\alpha_{opt,1}$ angles. The relative flow incident angle α_{s1} changes with the rotational speed, whereas the blade design parameters $\alpha_{opt,1}$ and $\alpha_{opt,2}$ remain fixed. Depending on the particular blade design and the rotational speed, the sign of Eq. (43) and hence, Eq. (44) can change. This can cause a saddle point of the vorticity wave amplitude in a variation of the rotational speed, which can be noted in the response of the acoustic energy transmission coefficient magnitude in Fig. 4. For entropy waves, the difference enters quadratically in Eq. (41) and hence, the sign is positive. This implies that the sign of the derivative terms in the Eqs. (42) and (44) is equal for some flow incidence angles. Therefore, a similar perturbation transmission behaviour (but at a different scale) is expected under certain inflow angles.[3]

Without vorticity and entropy waves, the acoustic energy transport characteristics remain approximately constant in the frequency range of interest (with typical blade dimensions of high-pressure compressors in gas turbines). Vorticity can be present in the mean flow. Contrary, entropy waves are not present in the mean flow; therefore, their wave amplitudes vanish in the zero-frequency limit. The generation of vorticity and entropy waves augments the frequency-dependency of the reflection characteristics due to the frequency-dependency of the delayed convection of total pressure (Eq. (42)) and flow angle perturbations (Eq. (44)) along blade passages. With the generation of vorticity waves, the, $p_1\left(\frac{\omega r}{a}+\beta_1 M_a\right)_1 C_{0,1}/p_2\left(\frac{\omega r}{a}+\beta_1 M_a\right)_2 C_{0,2}$, remain smaller than unity throughout the investigated frequency range. These pressure wave amplitude ratios exhibit similar values compared to those without vorticity waves. The transmission coefficient magnitude of the acoustic energy flux (with vorticity waves) can become larger than unity only with the multiplication of the mean flow contribution. The blade row loss coefficient has a more severe impact on the acoustic energy flux, leading to a significant increase in the acoustic energy transmission coefficient. Nonetheless, the delayed convection time plays an essential role for the acoustic energy flux resonance.

3.1. Axial compressor

In this section, the reflection characteristics are investigated with upstream excitation in a realistic application, i.e. an axial compressor with six stages. Its overall performance has been presented in Fig. 1. For all blade rows, the modelling coefficients A_1 and A_3 are set to 0.066 and 0.4, respectively, except when specified differently. The reflection and transmission coefficients are stated in this section as the ratio of the corresponding wave component to the incident upstream propagating wave at the compressor exit.

3.1.1. Effect of operating conditions on the reflection coefficients

The mean flow, the flow angles, and the pressure losses are different and, thereby, define the operating condition. Thus, the pressure reflection properties change for incident pressure waves at the compressor discharge, as illustrated in Fig. 5 for particular operating conditions defined in Fig. 1. The axial compressor model predicts approximately constant reflection coefficient amplitudes for the investigated frequency range at operating conditions near compressor choke (depicted by the orange lines). The estimated pressure reflection coefficients reveal significant frequency dependencies toward low mass-flow rate operating conditions.

The pressure reflection coefficient magnitudes obtained from an equivalent choked flow boundary condition (see C) are indicated by dotted lines and represent quantitatively reasonable estimates for operating conditions near compressor choke. However, these magnitudes do not strictly represent the upper bound (covering the worst-case scenario). For lower mass-flow rate operating conditions, the approximation of the reflection coefficient with the equivalent choked flow boundary condition is questionable because of the significant variations predicted with the present compressor model (e.g. the red or black lines). Moreover, the formulation of this compact choked flow boundary condition does not permit the prediction of a phase delay. Further, it was assumed that mass-flow rate and stagnation enthalpy perturbations vanish at the compressor discharge. However, the computed values for mass-flow rate and stagnation enthalpy perturbations with the compressor model normalised by their mean-flow value reach maximal values of approximately 15% and 40%, respectively. (Noteworthy is that the present model does not account for entropy dissipation effects.) Stow et al. [6] predicted a significant entropy wave generation at the inlet boundary with an effective length for the phase correction of the choked flow boundary condition.

[3] For perturbations passing a stator with pressure loss, the term, $\left(p'_{0,1}-p'_1\right)\overline{\varepsilon_L}$, in Eq. (44) governs the amplitude change. In contrast, the derivative terms become dominant for high rotational speeds.

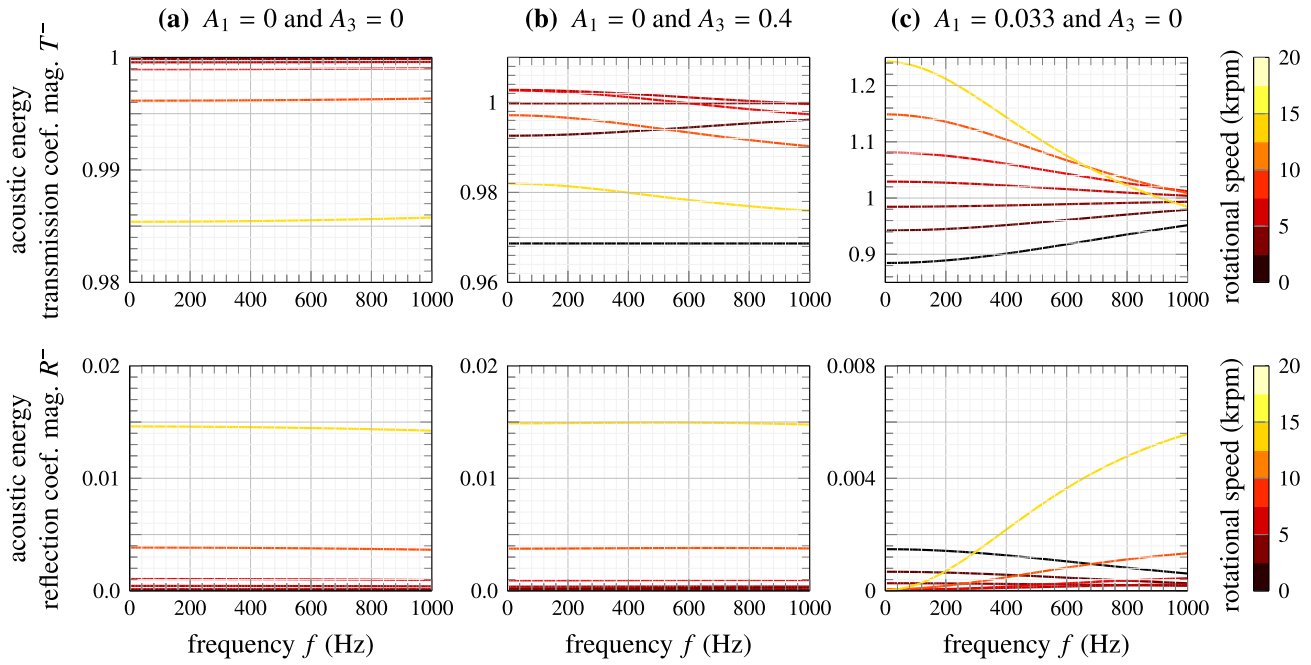

Fig. 4. Acoustic energy transmission (top row) and reflection (lower row) coefficient magnitudes are compared for different configurations of a single, 12° inclined blade row subjected to planar upstream excitation, where the cord length is 20 mm and the Mach number straight incoming flow is 0.3. The optimal incidence angle, $\alpha_{opt,1}$, is 38° and the optimal discharge angle, $\alpha_{opt,2}$, is 0°. The colours indicate the rotational speeds, which are varied from 0 to 20 krpm.

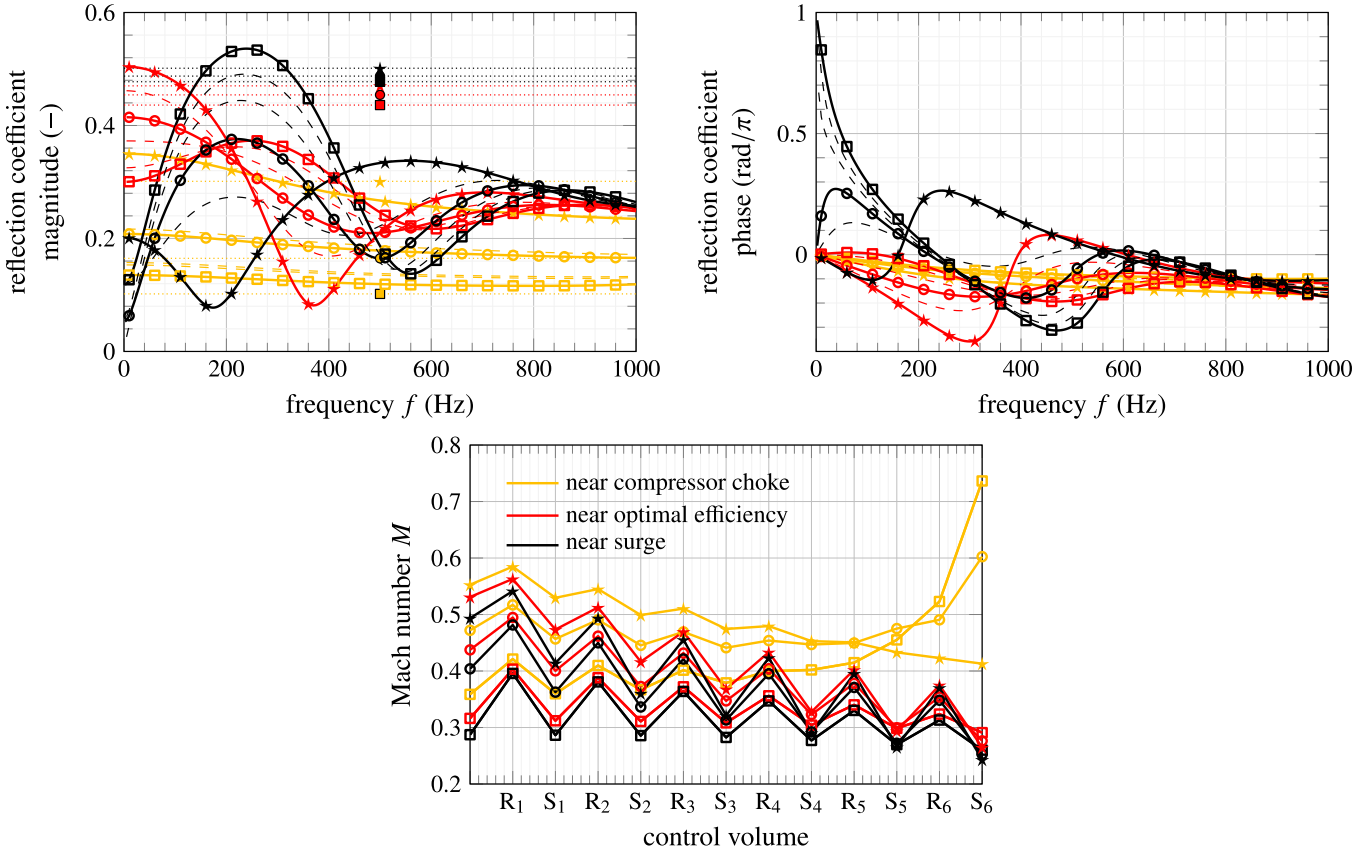

Fig. 5. The pressure reflection coefficient ($n = 0$) calculated at the compressor outlet is presented. The orange, red, and black coloured graphs correspond to the operating conditions near compressor choke, optimal operating conditions, and near surge, respectively. The symbols □, ○, and ★ indicate the 80%, 95% and 105% speed line of the compressor, respectively. The corresponding operating conditions are indicated on the compressor map shown in Fig. 1. The magnitudes obtained with the equivalent choked flow boundary condition are indicated as dotted lines in the corresponding colour code. (For interpretation of the references to colour in this figure legend, the reader is referred to the web version of this article.)

Fig. 6 shows the sequence of the complex coefficients, i.e. B_n and C_n, and illustrates where waves are transmitted and reflected at each stage in the compressor. The wave propagation pattern evolves distinct for near compressor choke operating conditions.[4] The wave amplitudes entering the compressor discharge decay rapidly within a few stages and cannot penetrate deep into the compressor. Reflection occurs primarily at the last blade rows, where the Mach number becomes high for such operating conditions. Fig. 5 shows that the Mach number increases even over stators near compressor choke since the flow incidence angles in these passages become extremely steep. The thereby induced stall cells inhibit the conversion of kinetic into pressure energy. After a certain penetration length, the reflection causes the approximately frequency-independent pressure reflection coefficients described in the previous paragraphs.

Lower flow velocities permit pressure waves to penetrate further into and even throughout the compressor. When interacting with blade rows, upstream travelling waves cause downstream propagating perturbations. Especially for low mass-flow rate conditions at high rotational speed, local wave amplitude intensifications, forming standing wave patterns, can be observed in the interior of the compressor. Noteworthy is that waves propagate less deep into the compressor at higher frequencies ($>$ 600 Hz).

3.1.2. Effect of the compressor characteristic slope on the reflection coefficients

Three compressor characteristics are generated by adapting the deviation factor, A_3, (for all blade rows) to investigate the impact of their steepness on the acoustic reflection behaviour beyond the zero-frequency limit. This modelling coefficient governs the proportionality of the flow deviation angle at the trailing edge with respect to the flow incidence angle and affects, thereby, the vorticity generation. Fig. 7 shows in the left column the predicted compressor performance for a variation of deviation factors at the 95% speed line. Lower deviation factors lead to steeper decreasing characteristics as compared with higher values. To focus solely on the slope (at a fixed speed line), an operating point is selected (marked by a black square) at which the three characteristics exhibit the same pressure ratio and efficiency. (The compressor efficiency remains unchanged for this operating point because the total pressure loss factor, A_1, is equal for all three generated compressor characteristics.) The changes of reflection coefficient magnitudes, shown in Fig. 7, can be mainly observed at low frequencies ($<$ 500 Hz), whereas phase delay alterations occur primarily in the mid-frequency range.

The cause for the different reflection coefficients can be found by inspecting Fig. 8, showing the complex coefficient distributions over the compressor stages. Vorticity waves are generated when upstream and downstream propagating waves at the trailing edge do not satisfy the Kutta condition. The flow deflection angle, determining the Kutta condition, is set proportionally by the deviation factor to the incidence angle. Fig. 8 shows clearly that the deviation factor scales the vorticity wave amplitudes, which evolve differently for the variation of deviation factor values. The alternating rotor and stator blade inclinations induce vorticity waves with opposite signs. The vorticity wave amplitudes can reach values close to zero downstream of stators for large flow angle perturbation damping, i.e. low deviation factors.

Higher deviation factors propagate more flow angle perturbations downstream. The change in the flow deflection angle can cause an intensification of upstream travelling waves by impairing the Kutta condition. Thereby, the higher deviation factors propagate the upstream travelling waves further into and even throughout the compressor, whereas the upstream wave propagation decays faster with a low deviation factor. The deterioration of the Kutta condition generates further amplified downstream propagating waves (by reflections) and entropy waves generated when vorticity waves do not balance the mismatch of upstream and downstream propagating waves at the trailing edge condition. Hence, the vorticity wave amplitudes remain high also downstream of stators in such scenarios.

Noteworthy are the similarities in the distribution of complex coefficients with altered deviation factors and near-optimal operating conditions at different speed lines. Figs. 6 and 8 show that a high deviation factor leads to similar complex coefficient distributions as a near-optimal operating condition on a higher speed line and vice versa.[5] However, the compressor characteristics are steeper on higher than on lower speed lines, which would suggest the opposite correlation. A comparison of the loss coefficient, shown in Fig. 9 as a function of the compressor stages, for three deviation factors and higher and lower speed lines reveals trends explaining the similarities of the constant coefficients. Clearly, an operating point on a higher or lower speed line has a similar loss coefficient distribution among the blade rows as a higher or lower deviation factor, respectively. The blade row pressure loss coefficient is related to the incident flow angle and thereby connected to the deviation factor of the preceding blade row. A low deviation factor (acting as a damper for flow angle disturbances) decreases the loss coefficient at the following blade row, while a high deviation factor increases the loss coefficient. Therefore, the observed relation of the complex coefficients is not unexpected. The leaving angle and pressure loss fluctuations relate to incident flow angle changes similar but opposite signs in the present model. This demonstrates that the reflection behaviour of the compressor depends not only on the partial derivative of the corrected mass-flow rate but also on the partial derivative of the rotational speed (as demonstrated in A). As applied in the present example, the variation of the deviation factor represents the partial derivative of the corrected mass-flow rate. Neglecting the partial derivative of the rotational speed can therefore lead to wrong reflection coefficient estimations.

Generally, changes of A_1, governing the total pressure loss coefficient magnitude, impact the wave transmission and reflection characteristics as changes in the deviation factor. Moreover, the impact of a deviation factor change at an individual blade row on the pressure reflection coefficient can be expected to scale with the provoked alteration of the loss coefficient amplitude at the consecutive blade row. Loss coefficient amplitudes are less affected at blade rows where the actual flow incidence angle is close to the optimal flow incidence angle. The occurrence of such scenarios (at particular stages) depends on the compressor operating conditions. Under surge operating conditions, the leading stages are mostly stalled, whereas the rearmost stages are commonly stalled close to compressor choke. Therefore, general statements for individual blade row importance can hardly be made.

Fig. 9 shows operating points for which a minimal loss coefficient (and hence, the least actual to optimal flow incidence angle difference) is reached at the second and third stages. Deviation factor changes at these individual blade rows generally have a less

[4] The complex coefficient contours shown in Fig. 6 have been scaled by the forcing amplitude, i.e. the upstream propagating wave entering at the compressor discharge. Thus, the penetration depth of the upstream propagating wave can be determined by the magnitude decay of the complex coefficient over the gap and blade control volumes towards the compressor inlet. The standing wave patterns can be noted as amplifications of the complex coefficients larger than one and hence, larger than the forcing amplitude.

[5] The complex coefficients shown in Fig. 8 for a deviation factor of 0.4 correspond to the complex coefficients shown in Fig. 6 for the speed line 95% at the near-optimal efficiency operating condition. The complex coefficients representing the upstream and downstream propagation can be compared for other speed lines and deviation factors.

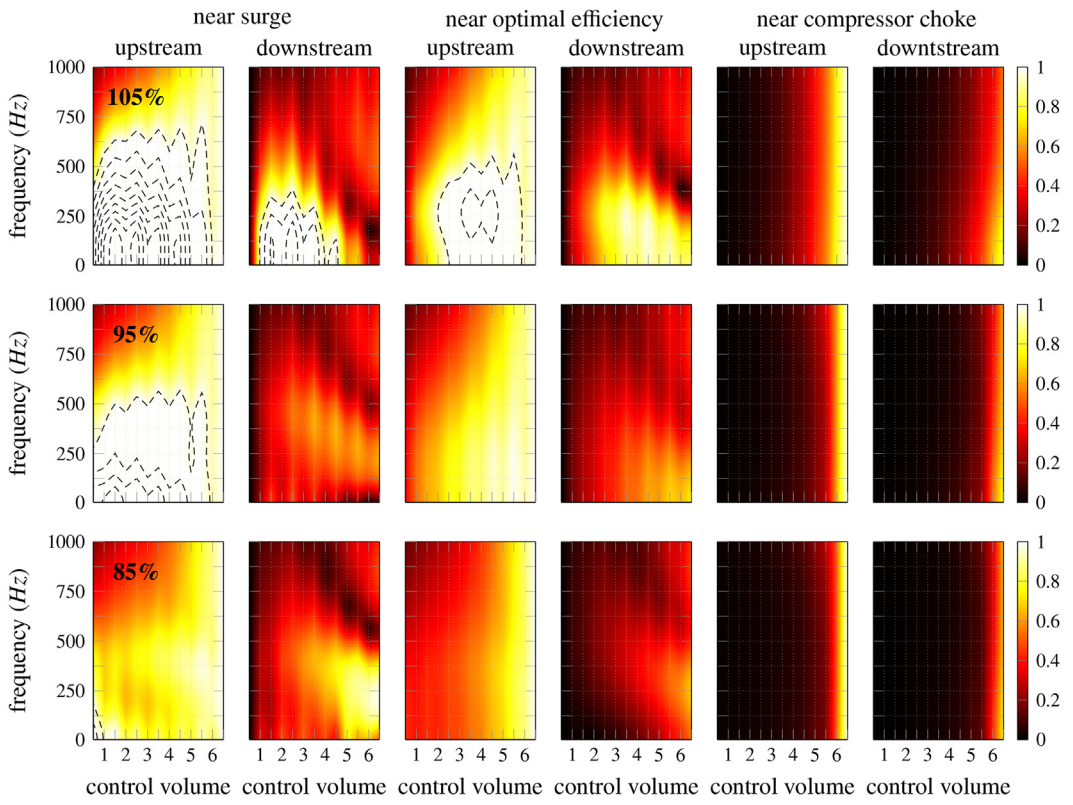

Fig. 6. The evolution of the complex coefficients B_n and C_n corresponding respectively to upstream and downstream propagation are shown for each gap and blade row control volume as function of speed line and operating condition accordingly to Fig. 1. (All complex coefficients are scaled such that the incident upstream propagating wave is unity at the compressor discharge. Dashed contour lines at amplitude intervals of 0.25 indicate complex coefficient amplitudes larger than unity.)

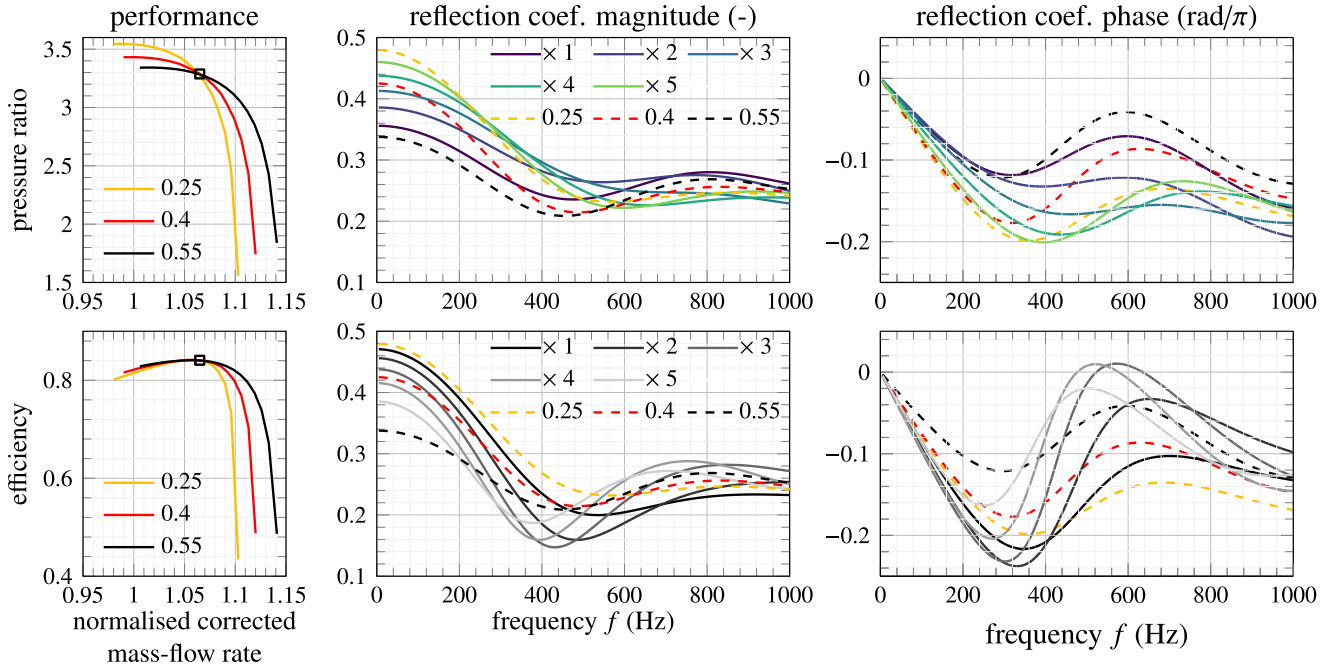

Fig. 7. Left column: Speed lines with three deviation factors, i.e. 0.25 (orange), 0.4 (red), and 0.55 (black). Middle and right column: Pressure reflection coefficients in terms of magnitude and phase for variations of deviation factors. The top row represents an initial state of a deviation factor of 0.55 over all blade rows, while altering successively the deviation factor for entire stages to 0.25 starting from the compressor discharge towards the inlet. The lower row shows the same procedure starting with a deviation factor of 0.25 altered successively to a deviation factor of 0.55. The colour code indicates the number of stages altered. (For interpretation of the references to colour in this figure legend, the reader is referred to the web version of this article.)

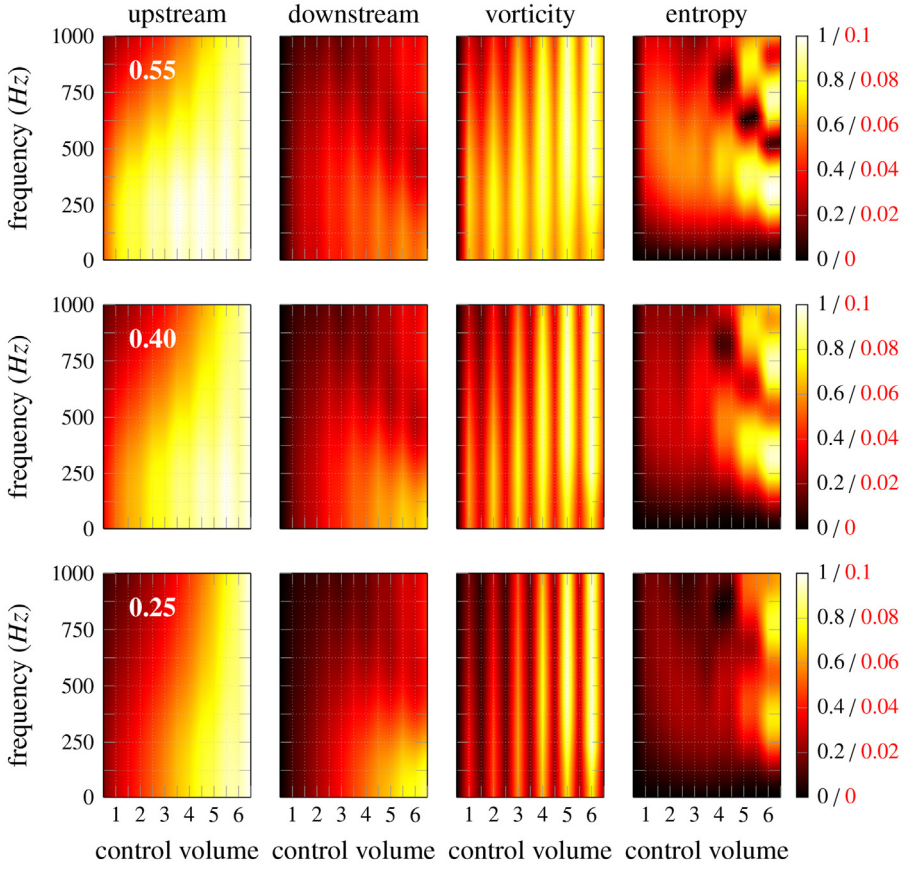

Fig. 8. The propagation properties of the compressor model with different deviation factors, i.e. 0.25, 0.4, and 0.55, (on the 95% speed line) are illustrated in terms of the complex coefficients. The amplitude scale shown in red corresponds only to the entropy waves.

significant impact on the pressure reflection coefficient. Further, the stator row at the compressor exit cannot affect any consecutive blade rows, and hence, the reflection coefficients are unaffected by alterations of the deviation factor of this last blade row.

Worthwhile to note is that the pressure reflection coefficient phase changes significantly depending on the particular arrangement of deviation factors, as shown in Fig. 7. Decreasing consecutively of the deviation factor causes a flat phase development, whereas a successive increase results in large phase variations.

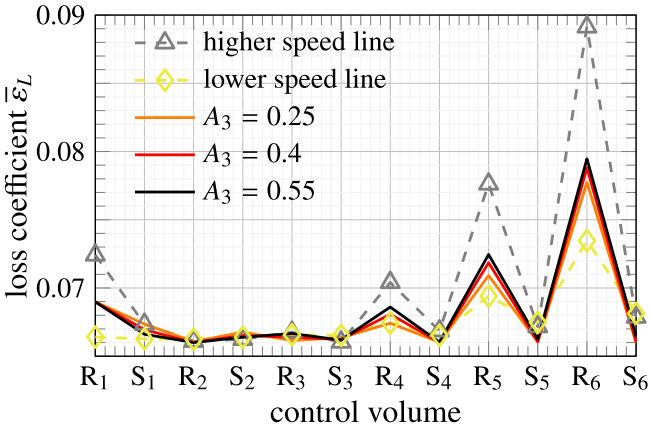

Fig. 9. The loss coefficient is compared for three deviation factors, i.e. 0.25, 0.4, and 0.55, on the 95% speed line to higher and lower speed lines.

These variations can outreach the reflection coefficients obtained with uniform deviation factors. Hence, the reflection coefficients obtained with uniform deviation factor distributions do not represent strict bounds.

3.2. Thermo-acoustic stability prediction

We show the impact of the compressor boundary condition in an applied thermo-acoustic stability calculation. The annular laboratory burner designed and described by Worth et al. [23] is investigated with an acoustic network approach. A schematic of the annular burner representation is illustrated in Fig. 10 (a), which shows that the combustor consists of an upstream plenum, 18 circumferentially equidistant distributed supply pipes, 18 flames, and a downstream plenum. A total pressure loss coefficient, $\zeta = (p_{0,1} - p_{0,2})/(1/2 \cdot \varrho u_a^2)$, corresponding to the experimental setup is applied at the flame holder.[6] In the experiment, a choked flow inlet condition applies. We illustrate how the potential presence of a compressor upstream of the combustor affects thermo-acoustic stability.

The focus of the present work is on the formulation of the axial compressor model to represent the upstream acoustic boundary condition of a combustor. Therefore, only the fundamental characteristics of the utilised acoustic network approach for thermo-acoustic stability prediction are described; more details have been provided by Stow et al. [24]. An investigated geometry is divided

[6] The validity of the general conclusions has been confirmed for values of the total pressure loss coefficients over 40.

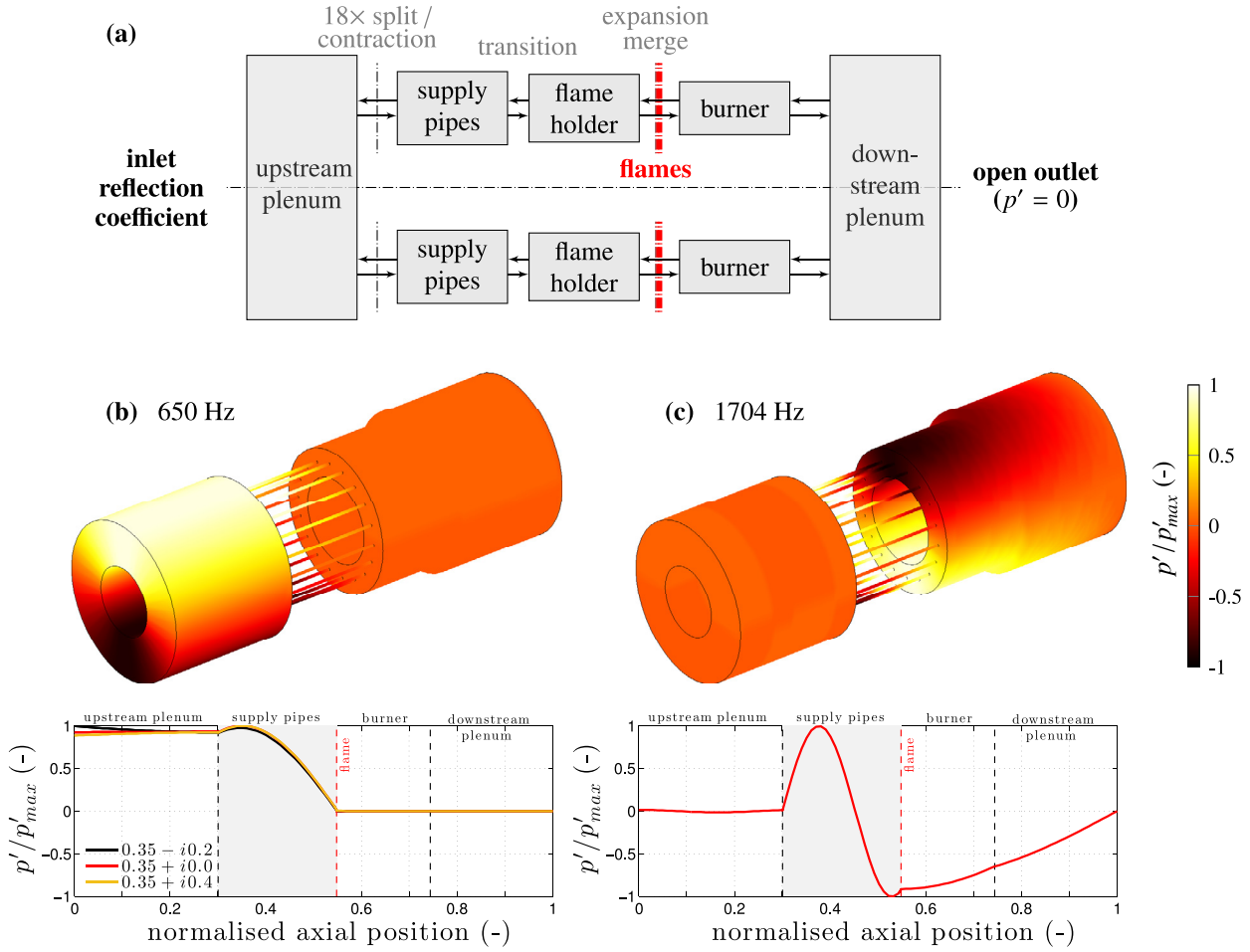

Fig. 10. The acoustic network model for the laboratory combustor developed by Worth et al. [23] is shown on the top. The grey shaded elements represent wave propagation blocks, the arrows are interface conditions, and the boundary conditions are stated at the sides. The shapes of the pressure perturbation generated by the two dominant circumferential modes ($p' = f(x)\ e^{i\omega t + in\theta}$ where $n = 1$) are illustrated on the below, where a three-dimensional visualisation is shown above the normalised one-dimensional pressure perturbation.

into one- or two-dimensional (acoustic) propagation-alike segments. Jump conditions join the segments of a network. For the low-order representation, the cross-sectional extensions of the combustor in the radial direction are assumed to be small compared to the perturbation wavelength. All primary variables are decomposed into time-averaged mean and fluctuating contributions. The mean flow quantities are calculated first with the inlet and outlet conditions known at the domain boundaries. The perturbations are then superimposed onto the mean flow. The transmission of the fluctuations, i.e. a vorticity wave, an entropy wave, and two acoustic waves, is governed by the cross-sectional area, radius, and length of the segment. Using the conservation equations, i.e. mass, momentum, and energy, the transformations to the perturbation amplitude of the fluxes can be obtained, which are used to apply appropriate expansion and contraction jump conditions. Linearised equations govern the propagation of perturbations except at the flame, which represents the essential non-linearity of the combustor system. For clarity, the simplistic $n - \tau$ model for the heat release response of the flame is utilised in the present calculations.

With the network approach, waves with frequencies and growth rates in certain ranges of interest are propagated from the inlet to the outlet. When the state of the wave matches the specified conditions imposed at the outlet, the error at this boundary vanishes, and a modal solution is found.

Worth et al. [23] focused on the most prominent circumferential resonant mode and reported its frequency at approximately 1.7 *kHz*, which increased with elevated equivalence ratio. Other amplified fluctuations have been identified in the range of 600 to 800 Hz and 1900 to 2000 Hz. With the acoustic network model for this configuration and a choked flow boundary condition at the inlet, the most unstable circumferential mode is predicted at a frequency of 1704 Hz. The second circumferential mode is marginally stable at 650 Hz.

The shape of the resonant modes, shown in Fig. 10 (b) and (c), clarifies their sensitivity to boundary conditions. An open exit boundary condition is employed at the combustor exit, i.e. $p' = 0$. The mode at a frequency of 1704 Hz has high fluctuation amplitudes in the supply pipes, the burner and the downstream plenum. The one-dimensional pressure perturbation plotted in Fig. 10 (c) shows clearly that the fluctuation amplitudes remain insignificant in the upstream plenum. Therefore, the inlet reflection coefficient has a minor effect on the growth rate of this mode.

On the contrary, the resonant mode at approximately 650 Hz exhibits high-pressure fluctuation magnitudes from the burner orifice to the inlet boundary, as shown in Fig. 10 (b). Therefore, the

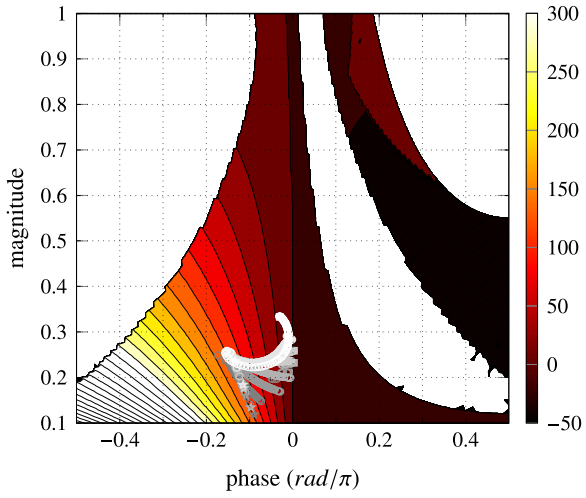

Fig. 11. Obtained growth rates of the mode at approximately 650 Hz for a variation of refection coefficients. In transparent areas, no mode solution is found. The symbols indicate reflection coefficients obtained for the compressor boundary condition model at different operating conditions (the white (105%) to grey (80%) colour indicates the speed line). At the ends, the squares and stars mark the near surge and compressor choke operating conditions, respectively.

growth rates of this mode are susceptible to changes of the reflection properties assigned at the inlet, which is more elaborately shown as a function of reflection coefficient magnitude and phase in Fig. 11. It can be observed that the growth rates are negative for this mode when the phase of the reflection coefficient is positive, while growth rates become positive for negative phase values. The mode shape changes slightly for different growth rates (see Fig. 10), and the frequency adjusts.

The obtained reflection coefficients with the compressor model are indicated in Fig. 11 for different operating conditions by white and grey symbols. Compressor choke can be identified as an operating condition prone to cause the unstable mode. Further, it may be noted that the path of predicted reflection coefficients along speed lines does not follow a straightforward trend, which might be predictable with a few samples. Worthwhile to note is that the growth rates do not significantly change for reflection coefficients with zero phase components. Therefore, the equivalent choked flow boundary condition will lead to a prediction of a marginally stable growth rate independently of its reflection coefficient amplitude. Although the reflection coefficient magnitudes were found to be similar for the equivalent choked flow and compressor choke reflection coefficients, the impact of the phase on the thermo-acoustic stability is decisive.

Amplification due to positive interference can only occur if the unsteady heat release rate and the acoustic perturbations are in phase. The importance of the phase criterion for the prediction of thermo-acoustic stability is shown in Fig. 11. Its relevance has been demonstrated by Bothien et al. [3], who studied the effect of inlet boundary conditions on thermo-acoustic instabilities in lean-premixed swirl burner. It could be shown that thermo-acoustic oscillations can be reduced through feedback control actuating the inlet impedance. Further, Silva et al. [9] (although employing a compact assumption for the individual centrifugal compressor stages) found with their thermo-acoustic stability calculations that the phase shift is the most influential factor while the reflection coefficient magnitude is of secondary importance.

4. Conclusions

To improve the representation of the real application in thermo-acoustic simulations, we developed a non-compact boundary condition mimicking the axial compressors by a low-order model. Control volumes represent each blade row and each gap between blade rows. The interface conditions are based on conservation equations and performance modelling. With the initial outset of the compressor, the required input is available to set up the boundary condition. The formulation allows fast and accurate phase shift evaluation accounting for convective time scales of the perturbation transmission in the blade passages.

Varying the performance of the axial compressor within the limits of operating conditions, i.e. near surge to near compressor choke, the obtained reflection coefficients vary significantly and exhibited strong frequency dependencies. The analysis of wave transmission and reflection properties in the compressor interior revealed that the upstream travelling waves penetrate far into or even throughout the geometry. Further, wave reflections can cause internal resonance. Thus, the compressor impedance at its discharge is governed by wave interactions at all stages, which a compact nozzle flow boundary condition cannot represent.

The importance of the reflection coefficient phase on the thermo-acoustic stability prediction was demonstrated for an acoustic network simulation of an annular combustor. The analysis illustrated for which conditions the growth rate of a resonant mode is sensitive to boundary condition variations. Negative phase shifts lead to high growth rates, whereas positive phase shifts resulted in neutral stability or damping. The obtained phase shifts with the present compressor model mainly were negative for the investigated resonant mode. The intricate distribution of predicted reflection coefficients suggests that many transfer functions would be required to represent the compressor accurately.

In recent years, the boundary conditions for wave reflection at nozzle geometries have significantly improved. Nevertheless, most works focus on the combustor discharge guiding the perturbations into the turbine stages. According to the particular flow, assumptions have been made which might not apply to the combustor inlet. The penetration of upstream incident waves into the compressor is only significantly restricted at near compressor choke operating conditions. This behaviour could be potentially modelled with these nozzle boundary conditions (choked flow), e.g. by an effective length correction suggested by Stow et al. [6]. However, a compressor is unlikely to be operated in a gas turbine at operating conditions with such low efficiency.

Declaration of Competing Interest

The authors declare that they have no known competing financial interests or personal relationships that could have appeared to influence the work reported in this paper.

Acknowledgement

This work was conducted within the EU 7th Framework Project Joint Technology Initiatives – Clean Sky (AMEL-Advanced Methods for the Prediction of Lean-burn Combustor Unsteady Phenomena), project number: JTI-CS-2013–3-SAGE-06-009/ 641453. The authors acknowledge TU Wien Bibliothek for financial support through its Open Access Funding Programme.

Appendix A. Reflection coefficient estimation based on performance map data

Performance maps describe the achieved quasi-steady total pressure, p_0, and total temperature, T_0, rise of a compressor between inlet and outlet (indicated with indices 1 and 2, respectively), where

$$\frac{p_{0,2}}{p_{0,1}} = f\left(\frac{\dot{m}\sqrt{c_p T_0}}{p_{0,1}A}, \frac{N}{\sqrt{c_p T_0}}, Re, T_{0,1}\right) \tag{A.1}$$

and

$$\frac{T_{0,2}}{T_{0,1}} = g\left(\frac{\dot{m}\sqrt{c_p T_0}}{p_{0,1}A}, \frac{N}{\sqrt{c_p T_0}}, Re, T_{0,1}\right) \tag{A.2}$$

state their dependencies; i.e. the inlet flow function, corrected rotational speed, Reynolds number, and inlet total temperature. Tip clearance losses scale with the inlet total temperature and turbulence effects are represented by the Reynolds number. However, both parameters cannot be simply modelled with compressor performance map data and are therefore neglected for the reflection coefficient estimation. Logarithmic differentiation of these two equations provides conservation relations for total pressure and total temperature fluctuations between compressor inlet and outlet,

$$\frac{p'_{0,2}}{p_{0,2}} - \frac{p'_{0,1}}{p_{0,1}} = \frac{\dot{m}_c}{f}\frac{\partial f}{\partial \dot{m}_c}\left(\frac{\dot{m}'_{c1}}{\dot{m}_{c1}} + \frac{1}{2}\frac{T'_{0,1}}{T_{0,1}} - \frac{p'_{0,1}}{p_{0,1}}\right) - \frac{N_c}{f}\frac{\partial f}{\partial N_c}\left(\frac{1}{2}\frac{T'_{0,1}}{T_{0,1}}\right), \tag{A.3}$$

$$\frac{T'_{0,2}}{T_{0,2}} - \frac{T'_{0,1}}{T_{0,1}} = \frac{\dot{m}_c}{g}\frac{\partial g}{\partial \dot{m}_c}\left(\frac{\dot{m}'_{c1}}{\dot{m}_{c1}} + \frac{1}{2}\frac{T'_{0,1}}{T_{0,1}} - \frac{p'_{0,1}}{p_{0,1}}\right) - \frac{N_c}{g}\frac{\partial g}{\partial N_c}\left(\frac{1}{2}\frac{T'_{0,1}}{T_{0,1}}\right). \tag{A.4}$$

Additionally, the mass-flow rate fluctuations $\dot{m}'_c/\dot{m}_c = \rho'/\rho + v'/v$ need to be conserved over the compressor. This leads to the equation system,

$$\begin{pmatrix} \frac{\dot{m}'_{c2}}{\dot{m}_{c2}} \\ \frac{p'_{0,2}}{p_{0,2}} \\ \frac{T'_{0,2}}{T_{0,2}} \end{pmatrix} = \begin{pmatrix} 1 & 0 & 0 \\ \phi_{\dot{m}} & 1-\phi_{\dot{m}} & \frac{\phi_{\dot{m}}-\phi_{N_c}}{2} \\ \Lambda_{\dot{m}} & -\Lambda_{\dot{m}} & 1+\frac{\Lambda_{\dot{m}}-\Lambda_{N_c}}{2} \end{pmatrix} \begin{pmatrix} \frac{\dot{m}'_{c1}}{\dot{m}_{c1}} \\ \frac{p'_{0,1}}{p_{0,1}} \\ \frac{T'_{0,1}}{T_{0,1}} \end{pmatrix}, \tag{A.5}$$

where

$$\phi_{\dot{m}} = \frac{\dot{m}_c}{f}\frac{\partial f}{\partial \dot{m}_c} \quad , \quad \phi_{N_c} = \frac{N_c}{f}\frac{\partial f}{\partial N_c},$$
$$\Lambda_{\dot{m}} = \frac{\dot{m}_c}{g}\frac{\partial g}{\partial \dot{m}_c} \quad \text{and} \quad \Lambda_{N_c} = \frac{N_c}{g}\frac{\partial g}{\partial N_c}. \tag{A.6}$$

The corrected mass-flow rate $\dot{m}_c$ is $\dot{m}\sqrt{T_0}/p_0$ and the corrected speed N_c is $N/\sqrt{T_0}$. The values for the derivatives can be obtained from the data presented in Fig. 1. To obtain reflection coefficients, the perturbation quantities are rewritten as characteristic waves. The same decomposition procedure can be employed as described in Section 2.2 for one-dimensional propagation of complex coefficients. This leads to the equation system for upstream ($i = 1$) and downstream ($i = 2$) quantities,

$$\begin{pmatrix} \frac{\dot{m}'_{ci}}{\dot{m}_{ci}} \\ \frac{p'_{0i}}{p_{0i}} \\ \frac{T'_{0i}}{T_{0i}} \end{pmatrix} = \begin{pmatrix} 1-1/M_i & 1+1/M_i & 1 \\ (\gamma-1)(1-M_i)/\Gamma & (\gamma-1)(1+M_i)/\Gamma & -1/\Gamma \\ \gamma(1-M_i)/\Gamma & \gamma(1+M_i)/\Gamma & \gamma M_i^2/(2\Gamma) \end{pmatrix} \begin{pmatrix} B_i \\ C_i \\ E_i \end{pmatrix}, \tag{A.7}$$

where $\Gamma = 1 + (\gamma-1)/2M_i^2$. The complex coefficients B, C, and E represent the upstream and downstream propagation, and entropy waves, respectively. Investigating solely the effect of the compressor, no downstream propagating and entropy waves are present at the compressor inlet. The ratio of complex coefficients B_2/C_2 is the reflection coefficient shown in Fig. 1 for the present investigated compressor with vanishing length.

Appendix B. Verification

To verify the present implementation, a comparison to the investigation by Kaji et al. [13] using the actuator disk theory is performed. Upstream excited pressure waves have been studied in a plain mean flow (at 0° incidence) while interacting with a static, 60° inclined blade row. The wavenumber, k, has been linked to the cord length c by $kc = 2\pi$. The transmitted and reflected wave amplitude ratios have been investigated. The comparison shown in Fig. A.12 demonstrates that the results by Kaji et al. [13] (see Fig. 5 (a)) and the present implementation are identical.

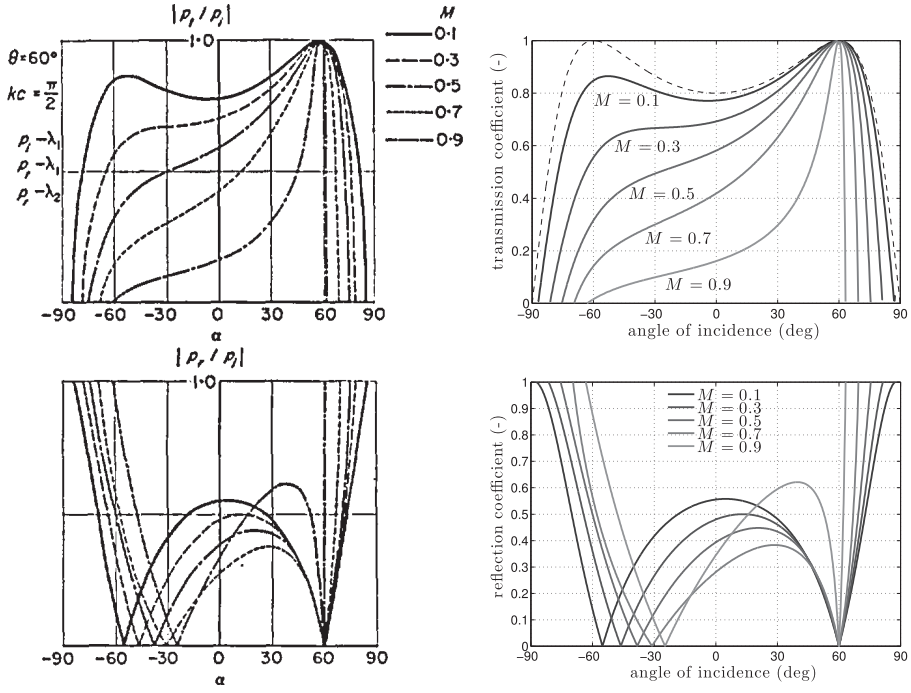

Fig. A.12. Comparison of the transmission and reflection coefficients calculated by Kaji et al. [13] (see Fig. 5 (a)) and with the present implementation.

Appendix C. Choked flow boundary condition

For this compact inlet boundary condition, the flow is assumed to be choked at the combustor entrance having a high velocity with a normal shock wave present. The gap is considered to be narrow compared to the perturbation wavelengths. With these assumptions, the mass-flow, total enthalpy, and vorticity perturbations are zero at this boundary. The condition for the mass-flow fluctuation $\dot{m}'$ can be formulated as,

$$\frac{\dot{m}'}{\dot{m}} = \frac{\rho'}{\rho} + \frac{v'}{v} = 0 \tag{C.1}$$

and the condition for the total enthalpy fluctuation h_0' using the ideal gas law, $p = \rho RT$, can be written as,

$$h_0' = c_p T' + v\ v' = c_p T\left(\frac{p'}{p} - \frac{\rho'}{\rho}\right) + v\ v' = 0. \tag{C.2}$$

The equivalent to these conditions can be computed at the compressor discharge for comparison. This requires that Eqs. (C.1) and (C.2) are satisfied at the compressor exit. This can be achieved by inserting Eqs. (14) and (16), divided by the axial Mach number M_a, into Eq. (C.1), and adding the condition for the total enthalpy fluctuation h_0',

$$h_0' = c_p(\gamma-1)\left(\frac{\omega r}{a}\left(B_n e^{i\phi} + C_n e^{i\psi}\right) - \frac{1}{\gamma-1}E_n e^{i\chi} + \left(nM_a^2 + M_\theta\left(\frac{\omega r}{a} + nM_\theta\right)\right)D_n e^{i\xi}\right) = 0. \tag{C.3}$$

The ratio of complex coefficients for upstream and downstream traveling waves (neglecting vorticity terms) at the compressor discharge is,

$$\frac{B_n}{C_n} = -\frac{\frac{\gamma\omega r}{a} + \beta_1\left(M_a - \frac{1}{M_a}\right)}{\frac{\gamma\omega r}{a} + \beta_2\left(M_a - \frac{1}{M_a}\right)}. \tag{C.4}$$

This ratio can be inserted into Eq. (11) to calculate the equivalent pressure reflection coefficient for choked flow.

Appendix D. Terms in transmission matrices

The individual terms in the transmission matrices described in Section 2.4 are given for the leading and trailing edge;

$$b_{1,1} = \frac{\omega r}{a_j} + nM_{\theta j} + \beta_{1j}\left(M_{aj} - \frac{1}{M_{aj}}\right)$$

$$b_{1,2} = \frac{\omega r}{a_j} + nM_{\theta j} + \beta_{2j}\left(M_{aj} - \frac{1}{M_{aj}}\right)$$

$$b_{1,3} = n$$

$$b_{1,4} = 1$$

$$b_{2,1} = \frac{\omega r}{a_j}\frac{T_{0j}(\gamma-1)}{1+\frac{(\gamma-1)}{2}M_j^2}$$

$$b_{2,2} = \frac{\omega r}{a_j}\frac{T_{0j}(\gamma-1)}{1+\frac{(\gamma-1)}{2}M_j^2}$$

$$b_{2,3} = \frac{T_{0j}(\gamma-1)\left(nM_{aj}^2 + \left(\frac{\omega r}{a_j} + nM_{\theta j}\right)M_{\theta j}\right)}{1+\frac{(\gamma-1)}{2}M_j^2}$$

$$b_{2,4} = \frac{-T_{0j}}{1+\frac{(\gamma-1)}{2}M_j^2}$$

$$b_{3,1} = \frac{\omega r}{a_j}\frac{p_{0j}\gamma}{1+\frac{(\gamma-1)}{2}M_j^2}$$

$$b_{3,2} = \frac{\omega r}{a_j}\frac{p_{0j}\gamma}{1+\frac{(\gamma-1)}{2}M_j^2}$$

$$b_{3,3} = \frac{p_{0j}\gamma\left(nM_{aj}^2 + \left(\frac{\omega r}{a_j} + nM_{\theta j}\right)M_{\theta j}\right)}{1+\frac{(\gamma-1)}{2}M_j^2}$$

$$b_{3,4} = \frac{p_{0j}\gamma M_j^2}{2+(\gamma-1)M_j^2}$$

$$c_{1,1} = 1 - \frac{1}{M_{\xi j+1}}$$

$$c_{1,2} = 1 + \frac{1}{M_{\xi j+1}}$$

$$c_{1,3} = 1$$

$$c_{2,1} = \frac{T_{0j+1}(\gamma-1)(1-M_{\xi j+1})}{1+\frac{1}{2}(\gamma-1)M_{\xi j+1}^2}$$

$$c_{2,2} = \frac{T_{0j+1}(\gamma-1)(1+M_{\xi j+1})}{1+\frac{1}{2}(\gamma-1)M_{\xi j+1}^2}$$

$$c_{2,3} = \frac{-T_{0j+1}}{1+\frac{1}{2}(\gamma-1)M_{\xi j+1}^2}$$

$$c_{3,1} = \frac{p_{0j+1}\gamma(1-M_{\xi j+1})}{1+\frac{1}{2}(\gamma-1)M_{\xi j+1}^2}$$

$$c_{3,2} = \frac{p_{0j+1}\gamma(1+M_{\xi j+1})}{1+\frac{1}{2}(\gamma-1)M_{\xi j+1}^2}$$

$$c_{3,3} = \frac{p_{0j+1}\gamma M_{\xi j+1}^2}{2+(\gamma-1)M_{\xi j+1}^2}$$

$$d_{1,1} = \frac{\omega r}{a_{j+2}} + nM_{\theta j+2} + \beta_{1j+2}\left(M_{aj+2} - \frac{1}{M_{aj+2}}\right)$$

$$d_{1,2} = \frac{\omega r}{a_{j+2}} + nM_{\theta j+2} + \beta_{2j+2}\left(M_{aj+2} - \frac{1}{M_{aj+2}}\right)$$

$$d_{1,3} = n$$

$$d_{1,4} = 1$$

$$d_{2,1} = \frac{\omega r}{a_{j+2}}\frac{T_{0j+2}(\gamma-1)}{1+\frac{(\gamma-1)}{2}M_{j+2}^2}$$

$$d_{2,2} = \frac{\omega r}{a_{j+2}}\frac{T_{0j+2}(\gamma-1)}{1+\frac{(\gamma-1)}{2}M_{j+2}^2}$$

$$d_{2,3} = \frac{T_{0j+2}(\gamma-1)\left(nM_{aj+2}^2 + \left(\frac{\omega r}{a_{j+2}} + nM_{\theta j+2}\right)M_{\theta j+2}\right)}{1+\frac{(\gamma-1)}{2}M_{j+2}^2}$$

$$d_{2,4} = \frac{-T_{0,j+2}}{1+\frac{(\gamma-1)}{2}M_{j+2}^2}$$

$$d_{3,1} = \frac{\omega r}{a_{j+2}} \frac{p_{0,j+2}\gamma}{1+\frac{(\gamma-1)}{2}M_{j+2}^2}$$

$$d_{3,2} = \frac{\omega r}{a_{j+2}} \frac{p_{0,j+2}\gamma}{1+\frac{(\gamma-1)}{2}M_{j+2}^2}$$

$$d_{3,3} = \frac{p_{0,j+2}\gamma\left(nM_{a,j+2}^2 + \left(\frac{\omega r}{a_{j+2}} + nM_{\theta,j+2}\right)M_{\theta,j+2}\right)}{1+\frac{(\gamma-1)}{2}M_{j+2}^2}$$

$$d_{3,4} = \frac{p_{0,j+2}\gamma M_{j+2}^2}{2+(\gamma-1)M_{j+2}^2}$$

$$d_{4,1} = -\left(\frac{\beta_{1,j+2}}{M_{a,j+2}} - \frac{n}{M_{\theta,j+2}}\right)\frac{\tan(\alpha_{s,j+2})}{1+\tan^2(\alpha_{s,j+2})}$$

$$d_{4,2} = -\left(\frac{\beta_{2,j+2}}{M_{a,j+2}} - \frac{n}{M_{\theta,j+2}}\right)\frac{\tan(\alpha_{s,j+2})}{1+\tan^2(\alpha_{s,j+2})}$$

$$d_{4,3} = -\frac{\omega r}{a_{j+2}}\frac{\tan(\alpha_{s,j+2})}{1+\tan^2(\alpha_{s,j+2})}$$

$$d_{4,4} = 0$$

$$\Delta p_1 = \frac{-1}{1+i(\omega+n\Omega)\tau_j}\left(\overline{\varepsilon_{Lj}}\left(\frac{\omega r}{a_j}\frac{p_{0,j}\gamma}{1+\frac{(\gamma-1)}{2}M_j^2} - p_j\gamma\left(\frac{\omega r}{a_j}+nM_{\theta j}+\beta_{1,j}M_{aj}\right)\right)+ (p_{0j}-p_j)\left(\frac{\partial\overline{\varepsilon_{Lj}}}{\partial\tan(\alpha_{sj})}\tan(\alpha_{sj})\left(\frac{\beta_{1,j}}{M_{aj}}-\frac{n}{M_{\theta j}}\right)+\frac{\partial\overline{\varepsilon_{Lj}}}{\partial M_j}\left(-\beta_{1,j}\frac{M_{aj}}{M_j}-n\frac{M_{\theta j}}{M_j}-M_j\frac{\gamma-1}{2}\left(\frac{\omega r}{a_j}+\beta_{1,j}M_{aj}+nM_{\theta j}\right)\right)\right)\right)$$

$$\Delta p_2 = \frac{-1}{1+i(\omega+n\Omega)\tau_j}\left(\overline{\varepsilon_{Lj}}\left(\frac{\omega r}{a_j}\frac{p_{0,j}\gamma}{1+\frac{(\gamma-1)}{2}M_j^2} - p_j\gamma\left(\frac{\omega r}{a_j}+nM_{\theta j}+\beta_{2,j}M_{aj}\right)\right)+ (p_{0j}-p_j)\left(\frac{\partial\overline{\varepsilon_{Lj}}}{\partial\tan(\alpha_{sj})}\tan(\alpha_{sj})\left(\frac{\beta_{2,j}}{M_{aj}}-\frac{n}{M_{\theta j}}\right)+\frac{\partial\overline{\varepsilon_{Lj}}}{\partial M_j}\left(-\beta_{2,j}\frac{M_{aj}}{M_j}-n\frac{M_{\theta j}}{M_j}-M_j\frac{\gamma-1}{2}\left(\frac{\omega r}{a_j}+\beta_{2,j}M_{aj}+nM_{\theta j}\right)\right)\right)\right)$$

$$\Delta p_3 = \frac{-1}{1+i(\omega+n\Omega)\tau_j}\left(\overline{\varepsilon_{Lj}}\frac{p_{0,j}\gamma}{1+\frac{(\gamma-1)}{2}M_j^2}\left(nM_{aj}^2\left(\frac{\omega r}{a_j}+nM_{\theta j}\right)M_{\theta j}\right)+ (p_{0j}-p_j)\left(\frac{\partial\overline{\varepsilon_{Lj}}}{\partial\tan(\alpha_{sj})}\tan(\alpha_{sj})\frac{\omega r}{v_{\theta j}}+\frac{\partial\overline{\varepsilon_{Lj}}}{\partial M_j}\left(n\frac{M_{aj}}{M_j}-M_{aj}+\frac{M_{\theta j}}{M_j}\left(\frac{\omega r}{a_j}+nM_{\theta j}\right)\right)\right)\right)$$

$$\Delta p_4 = \frac{-1}{1+i(\omega+n\Omega)\tau_j}\left(\overline{\varepsilon_{Lj}}\frac{p_{0j}\gamma M_j^2}{2+(\gamma-1)M_j^2}+(p_{0j}-p_j)\frac{\partial\overline{\varepsilon_{Lj}}}{\partial M_j}\frac{M_j}{2}\right)$$

$$\Delta\alpha_{s,1} = \frac{-1}{1+i(\omega+n\Omega)\tau_j}\left(\frac{\partial\tan(\alpha_{s,j+2})}{\partial\tan(\alpha_{sj})}\frac{n+\frac{M_{aj}}{M_{aj}}\beta_{1,j}}{M_{aj}\left(1+\left(\frac{M_{\theta j}}{M_{aj}}\right)^2\right)}+ \frac{\partial\tan(\alpha_{s,j+2})}{\partial M_j}\left(\frac{-\beta_{1,j}-n\frac{M_{aj}}{M_{aj}}}{\sqrt{1+\left(\frac{M_{\theta j}}{M_{aj}}\right)^2}}-\frac{M_j(\gamma-1)}{2}\left(\frac{\omega r}{a_j}+nM_{\theta j}+\beta_{1,j}M_{aj}\right)\right)\right)$$

$$\Delta\alpha_{s,2} = \frac{-1}{1+i(\omega+n\Omega)\tau_j}\left(\frac{\partial\tan(\alpha_{s,j+2})}{\partial\tan(\alpha_{sj})}\frac{n+\frac{M_{aj}}{M_{aj}}\beta_{2,j}}{M_{aj}\left(1+\left(\frac{M_{\theta j}}{M_{aj}}\right)^2\right)}+ \frac{\partial\tan(\alpha_{s,j+2})}{\partial M_j}\left(\frac{-\beta_{2,j}-n\frac{M_{aj}}{M_{aj}}}{\sqrt{1+\left(\frac{M_{\theta j}}{M_{aj}}\right)^2}}-\frac{M_j(\gamma-1)}{2}\left(\frac{\omega r}{a_j}+nM_{\theta j}+\beta_{2,j}M_{aj}\right)\right)\right)$$

$$\Delta\alpha_{s,3} = \frac{-1}{1+i(\omega+n\Omega)\tau_j}\left(\frac{\partial\tan(\alpha_{s,j+2})}{\partial\tan(\alpha_{sj})}\frac{\frac{\omega r}{a_j}}{M_{aj}\left(1+\left(\frac{M_{\theta j}}{M_{aj}}\right)^2\right)}+\frac{\partial\tan(\alpha_{s,j+2})}{\partial M_j}\frac{nM_{aj}+\frac{M_{\theta j}}{M_{aj}}\left(\frac{\omega r}{a_j}+nM_{\theta j}\right)}{\sqrt{1+\left(\frac{M_{\theta j}}{M_{aj}}\right)^2}}\right)$$

$$\Delta\alpha_{s,4} = \frac{-1}{1+i(\omega+n\Omega)\tau_j}\frac{\partial\tan(\alpha_{s,j+2})}{\partial M_j}\frac{M_j}{2}.$$

References

[1] Dowling AP. The challenges of lean premixed combustion. In Proc. International Gas Turbine Congress (IGTC2003); 2003.

[2] Lamarque N, Poinsot T. Boundary conditions for acoustic eigenmodes computation in gas turbine combustion chambers. AIAA J 2008;46 (9):2282–92. https://doi.org/10.2514/1.35388.

[3] Bothien MR, Moeck JP, Paschereit CO. Active control of the acoustic boundary conditions of combustion test rigs. J Sound Vib 2008;318(4–5):678–701. https://doi.org/10.1016/j.jsv.2008.04.046.

[4] Motheau E, Nicoud F, Poinsot T. Using boundary conditions to account for mean flow effects in a zero mach number acoustic solver. J Eng Gas Turbines Power 134 (11). doi:10.1115/1.4007198.

[5] Marble F, Candel S. Acoustic disturbance from gas non-uniformities convected through a nozzle. J Sound Vib 1977;55(2):225–43. https://doi.org/10.1016/0022-460X(77)90596-X.

[6] Stow S, Dowling A, Hynes T. Reflection of circumferential modes in a choked nozzle. J Fluid Mech 2002;467:215–39. https://doi.org/10.1017/S0022112002001428.

[7] Duran I, Moreau S. Solution of the quasi-one-dimensional linearized euler equations using flow invariants and the magnus expansion. J Fluid Mech 2013;723:190–231. https://doi.org/10.1017/jfm.2013.118.

[8] Lohse S, Koch R, Moreau S, Fischer F, Seume JR. Aeroacoustic numerical investigation of a scaled compressor cascade. In Proceedings of Global Power and Propulsion Society (GPPS Chania20), no. GPPS-CH-2020-0094; 2020. pp. 1–10.

[9] Silva CF, Duran I, Nicoud F, Moreau S. Boundary conditions for the computation of thermoacoustic modes in combustion chambers. AIAA J 2014;52 (6):1180–93. https://doi.org/10.2514/1.J052114.

[10] Yeddula SR, Gaudron R, Morgans AS. Acoustic absorption and generation in ducts of smoothly varying area sustaining a mean flow and a mean temperature gradient. J Sound Vib 2021;515:. https://doi.org/10.1016/j.jsv.2021.116437116437.

[11] Hellmich B, Seume JR. Causes of acoustic resonance in a high-speed axial compressor. J Turbomach 2008;130(3):. https://doi.org/10.1115/1.2775487031003.

[12] Hynes T. Actuator and semi-actuator disk models of compression systems operating with inflow distortion, CUED/A – Turbo/TR 104.

[13] Kaji S, Okazaki T. Propagation of sound waves through a blade row: I. analysis based on the semi-actuator disk theory. J Sound Vib 1970;11(3):339–53. https://doi.org/10.1016/S0022-460X(70)80038-4.

[14] Knobloch K, Guerin S, Holewa A, Mahmoudi-Larimi Y, Hynes T, Bake F. Noise transmission characteristics of a high pressure turbine stage. In 22nd AIAA/CEAS Aeroacoustics Conference, AIAA 2016–3001, AIAA; 2016. p. 12. doi:10.2514/6.2016-3001.

[15] Rienstra SW. Impedance models in time domain, including the extended helmholtz resonator model. AIAA Paper 2006;2686:2006. https://doi.org/10.2514/6.2006-2686.

[16] Fung K-Y, Ju H. Broadband time-domain impedance models. AIAA J 2001;39 (8):1449–54. https://doi.org/10.2514/2.1495.

[17] Emmons H, Pearson C, Grant H, et al. Compressor surge and stall propagation. Trans ASME 1955;77(4):455–69. https://doi.org/10.1115/1.4014389.

[18] Mazzawy R. Multiple segment parallel compressor model for circumferential flow distortion. J Eng Power 1977;99(2):288–96. https://doi.org/10.1115/1.3446288.

[19] Lieblein S. Incidence and deviation-angle correlations for compressor cascades. J Basic Eng 1960;82(3):575–84. https://doi.org/10.1115/1.3662666.

[20] König W, Hennecke D, Fottner L. Improved blade profile loss and deviation angle models for advanced transonic compressor bladings. part 1: A model for subsonic flow. J Turbomach 1996;118:73–80. https://doi.org/10.1115/1.2836609.

[21] Banjac M, Petrovic MV, Wiedermann A. A new loss and deviation model for axial compressor inlet guide vanes. J Turbomach 2014;136(7):. https://doi.org/10.1115/1.4025956071011.

[22] Ferrer-Vidal LE, Schneider M, Allegretti A, Pachidis V. A loss and deflection model for compressor blading at high negative incidence. J Turbomach 141 (12). doi:10.1115/1.4044967.

[23] Worth NA, Dawson JR. Self-excited circumferential instabilities in a model annular gas turbine combustor: Global flame dynamics. Proc Combust Inst 2013;34(2):3127–34. https://doi.org/10.1016/j.proci.2012.05.061.

[24] Stow SR, Dowling AP. Thermoacoustic oscillations in an annular combustor. In ASME Turbo Expo 2001: Power for Land, Sea, and Air, no. 2001-GT-0037, American Society of Mechanical Engineers; 2001. pp. V002T02A004–V002T02A004. doi:10.1115/2001-GT-0037.